XMM

XMM-Newton Optical and UV Monitor (OM) Calibration Status

XMM-SOC-CAL-TN-0019 Issue 9.0

Simon Rosen, OMCal Team
XMM-Newton Science Operations Center

OMCal Team
MSSL-UCL

07 February 2025

Revision history

Revision number	Date	Revision author	Comments
3.2	24 June 2004	B. Chen and OMCal Team	last update in old format
4.0	25 July 2007	A. Talavera and OMCal Team	Reformatted document
5.0	30 October 2008	A. Talavera and OMCal Team	General update
6.0	20 January 2011	A. Talavera and OMCal Team	Update
7.0	07 September 2020	S. Rosen and OMCal Team	Update
8.0	27 September 2023	S. Rosen and OMCal Team	Update
9.0	07 February 2025	S. Rosen and OMCal Team	Update
9.0	07 February 2025	S. Rosen and OMCal Team	Update

Contents

1 Introduction **1**

2 Instrumental corrections **1**
2.1 Dark count rate . . . 1
2.2 Flat fields . . . 3
2.2.1 Damage by the Jupiter observation in revolution 3224 . . . 4
2.3 Bad pixels . . . 5
2.4 Operational modes, source detection and count rate . . . 8
2.5 Coincidence Loss . . . 8
2.6 Point Spread Function . . . 9
2.7 Distortion . . . 10
2.8 Large scale Sensitivity variation . . . 13
2.9 Background . . . 18
2.10 Straylight . . . 19
2.11 Fixed patterning . . . 19

3 OM simulations, Throughput, Effective Area and Zero-points **20**
3.1 In-flight throughput and time sensitivity degradation . . . 20
3.2 Effective areas and response matrices . . . 23
3.2.1 The White filter. . . . 24
3.3 Red leak in UV filters . . . 24
3.4 Sensitivity impact of the Jupiter patch . . . 25

4 OM Photometry **30**
4.1 Zero points . . . 30
4.2 UBV colour transformation . . . 30
4.3 UV colour transformation . . . 31
4.4 Testing OM photometry with data in SA95-42 field . . . 33
4.5 AB photometry system . . . 33

5 Absolute flux calibration of the OM filters (OM count rate to flux conversion) **35**

6 Fast mode **37**

7 OM Grisms **38**
7.1 Wavelength calibration . . . 39
7.2 Flux calibration . . . 40
7.3 Time-dependent degradation . . . 42
7.3.1 Impact of the Jupiter patch . . . 45

8 Current Calibration Files (CCFs) for SAS **47**

9 Future calibration plans **47**

10 Acknowledgments **48**

11 References **48**

12 Appendix A: Calibration stars **50**

13 Appendix B: Summary of errors and repeatability **51**

14 Appendix C: Flux steps in Fast mode and imaging photometry taken in default mode **51**

15 Appendix D: Differences between the time-dependent degradation seen in standards and OM catalogue sources **53**

16 Appendix E: Corrections for the additional degradation at the pn boresight **53**

ABSTRACT

This document reflects the status of the calibration of the OM instrument on board XMM-Newton. Instrumental corrections such as coincidence loss, time dependent sensitivity degradation, spatial distortion, fixed pattern noise, point spread function etc., are described. The instrumental photometric system is defined as well as transformations to the standard Johnson UBV. An AB system is also defined for all optical and ultraviolet filters. We show that a photometric repeatability within 3% RMS can be achieved with the OM. The astrometric accuracy is about 1 arcsec. Count rate to flux conversion factors have been derived based on observations of spectrophotometric standard stars. Both UV and optical grisms have been calibrated in wavelength and in flux. The impact of the reduced sensitivity 'Jupiter patch' is described. With the exception of the Jupiter patch, all corrections and calibrations are implemented into SAS. A summary of the errors of the calibration is given in Appendix B.
The main updates in this release compared to the previous issue 8.0, are in sections 3.1 and 3.4. and 7.3.

1 Introduction

The Optical Monitor extends the spectral coverage of the XMM-Newton observatory into the UV and optical, thus allowing the possibility to test models against data over a broad energy band and importantly, therefore, enhancing the achievable XMM-Newton science. It can provide arcsecond resolution imaging of the whole field of view and can simultaneously zoom into a small area to provide timing information. Six broad band filters allow colour discrimination, and there are two grisms, one in the UV and one in the optical, to provide low resolution spectroscopy.
A description of the instrument and some operational guidelines can be found in the XMM-Newton web pages:

`https://www.cosmos.esa.int/web/xmm-newton/technical-details-om`

`https://xmm-tools.cosmos.esa.int/external/xmm_user_support/documentation/uhb/`

More detailed information about the OM can be found in Mason et al. (2001). This report summarizes the OM calibration. The instrumental corrections are described. The OM photometric system is defined and its relation with the Johnson UBV standard is established. An AB system, particularly useful for the UV range is also defined. Count rate to absolute flux conversions are also defined for all filters, based in observations of spectrophotometric standards. These standards are used to define the absolute flux calibration of the grisms too.
Almost all the corrections as well as the calibration are implemented into SAS 21.0. However the methods, algorithms and implementation details are not the purpose of this document. Readers interested in a SAS description should refer to the corresponding guide and on line documentation at

`https://www.cosmos.esa.int/web/xmm-newton/sas`

2 Instrumental corrections

2.1 Dark count rate

The dark frames are long exposures (4000 seconds) obtained in full frame configuration (low or high resolution) in the Blocked filter wheel position.
The dark count rate is very low, of the order of 0.0004 count/s/pixel and its variation across the detector is of the order of 7%. Figure 1 shows the mean dark count rate as a function of time, which is being monitored routinely. Sometimes dark frames are obtained serendipitously when OM cannot be used scientifically due to the presence of bright sources in the field of view. The large outlier values visible in Figure 1 may be produced in these cases - the largest outliers correspond to observations containing bright optical sources. The cause of the long term variation is unclear but the apparent cyclic behaviour is broadly consistent with the 11-year solar cycle, the peaks of the dark count aligning, approximately with the troughs of the solar cycle.

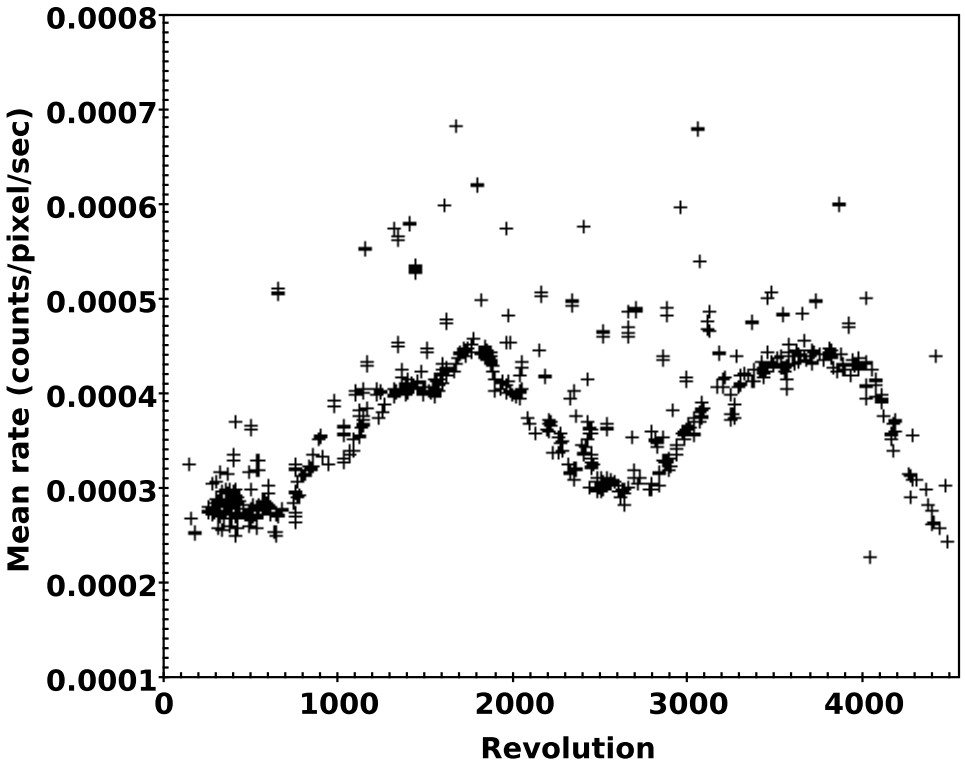


Figure 1: The mean dark count rate per (0.5 arcsec x 0.5 arcsec) pixel as a function of time, up to revolution 4500 (2024 July 04).

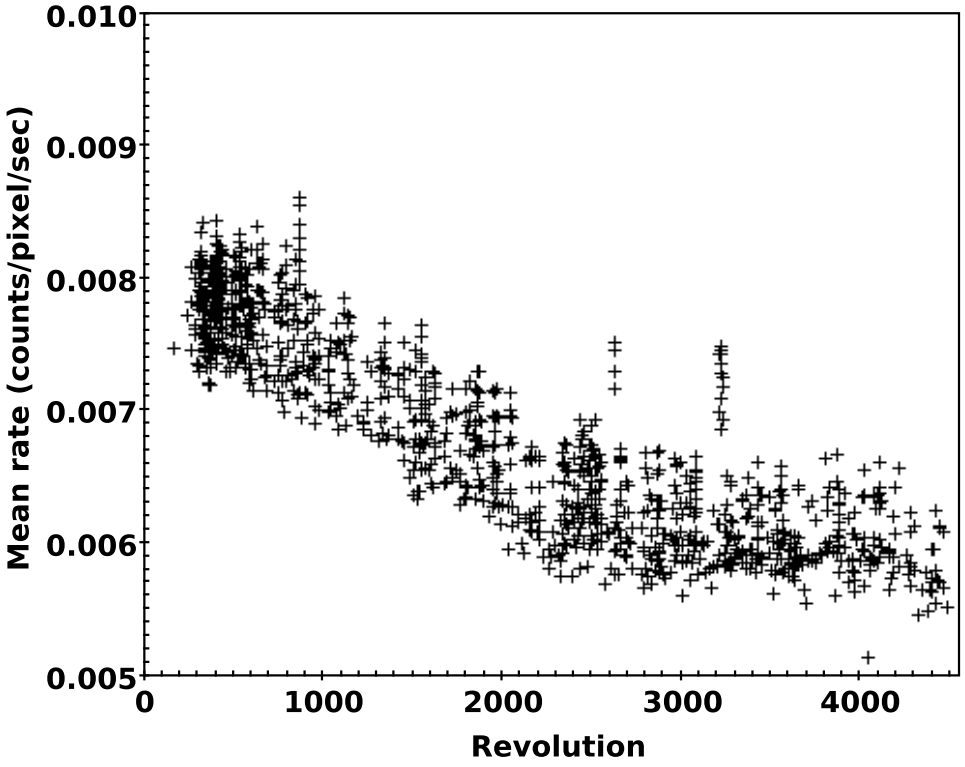


Figure 2: The mean flat field count rate per (0.5 arcsec x 0.5 arcsec) pixel, as a function of time, up to revolution 4500 (2024 July 04).

2.2 Flat fields

Flat field exposures are obtained also in full frame configuration (low or high resolution) with the filter wheel in Blocked position. A LED illuminates the back of the filter and the reflected light goes into the detector.
The LED illumination provided a count rate of 0.0078 count/s/pixel at the start of the mission, though it is not a uniform illumination. The mean count rate in the central part (10" × 10") of the detector as a function of time is shown in Figure 2. Super-flat fields have been produced during the life of the instrument. They typically include more than 80 hours of flat field time, therefore reaching the 2% statistical level. The comparison of these super-flats shows us that there are no large-scale (multi-pixel) areas of degradation on the detector, other than the Jupiter patch (see section 2.2.1).
After removing the illumination signature, the super-flat can be used to measure pixel to pixel non-uniformity caused by small-scale variations in the detector sensitivity over the field of view. The results of the photometry indicate that the pixel-to-pixel variation is less than 5%. Current SAS uses a unity flat field, since it does not affect the accuracy of the results by more than a few percent, except where sources are affected by the Jupiter patch.

2.2.1 Damage by the Jupiter observation in revolution 3224

On 2017 July 16 and 17 (revolution 3224), the OM was erroneously used during an XMM-Newton pointing of Jupiter (observation 0801930901), in which the planet was imaged with the V-band filter instead of the blocked filter.
As a consequence, the detector was exposed to over 2×10^8 photons/s during two, 4ks exposures, and suffered lasting damage to a small area. The damaged region is broadly elliptical in shape, covering some 19750 pixels (about 0.5% of the full detector) - see figure 3. It is centred (in unbinned pixels) at about 1110,910, with major and minor axes of 208 and 118 pixels ($\approx$ 105 and 60 arcsecs), respectively, and these pixels are identified in the bad pixel CCF (see section 2.3). Currently, during OM SAS processing, sources in the Jupiter patch, as defined in the bad pixel CCF, are only flagged (only for epochs > revolution 3224); they are not corrected for the loss of sensitivity. The effect of the damage is wavelength-dependent, being deepest in the V band, with measurements indicating a residual throughput, at the centre of the patch, of some 62%, 77%, 80%, 86%, 86% and 82% in the V, B, U, W1, M2 and W2 filters respectively. It should be noted, as discussed further in section 3.4, that the region of bad pixels defined for the Jupiter patch in the CCF does not, in fact, cover the entire affected region. The pn boresight, where most targets are observed, lies slightly outside the currently defined Jupiter patch badpixel region but within the shallow, outer parts of its wings, and suffers some reduction of sensitivity. The degradation in the Jupiter patch, particularly at the pn boresight location, is regularly monitored via observations of standard stars. Current data suggest the pn boresight sensitivity is continuing to decline slowly. Options for fully characterising and correcting for the degradation are being considered.

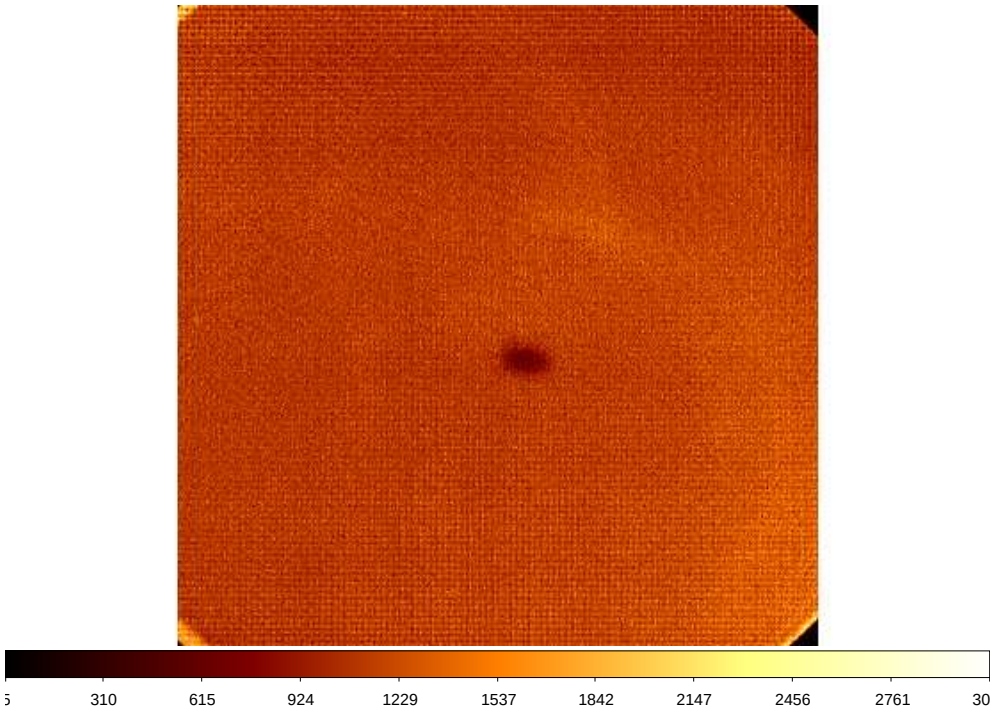


Figure 3: Full frame flatfield image from a stack of flats taken after revolution 3224. The Jupiter patch can be seen as the dark elliptical region near the centre

2.3 Bad pixels

The OM CCD has a usable area of 256 × 256 physical pixels for science observation. The detector achieves a large format of 2048 × 2048 sub-pixels through a centroiding technique, which measures the position of incident photons with a resolution of 1/8 of a physical pixel (see XMM-Newton User Handbook for details). From the super-flat mentioned above, we are able to recognize bad pixels. Moreover, some observations on very extended objects, such as comets, are used to identify low sensitivity pixels.
Figure 4 shows a bad pixel in the detector (x,y) = (866, 176), and Table 1 shows the coordinates of the bad and low sensitivity pixels (position of the central sub-pixel of the affected area). Their spatial distribution can be seen in figure 5. The origin for OM bad pixel coordinates is (1,1) and the size is (2048,2048). In general, the OM detector is good, with few bad pixels. These bad pixels have been recorded in the bad pixel CCF, and data taken in the area of bad pixels are flagged by SAS as being of potentially poor quality. The elliptical patch near the centre is the Jupiter patch which is discussed in section 2.2.1.

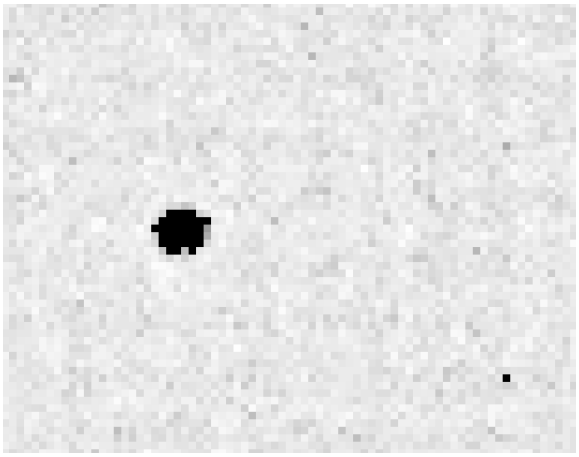


Figure 4: A bad pixel (x,y)=(866,176) can be seen clearly from the super-flat frame

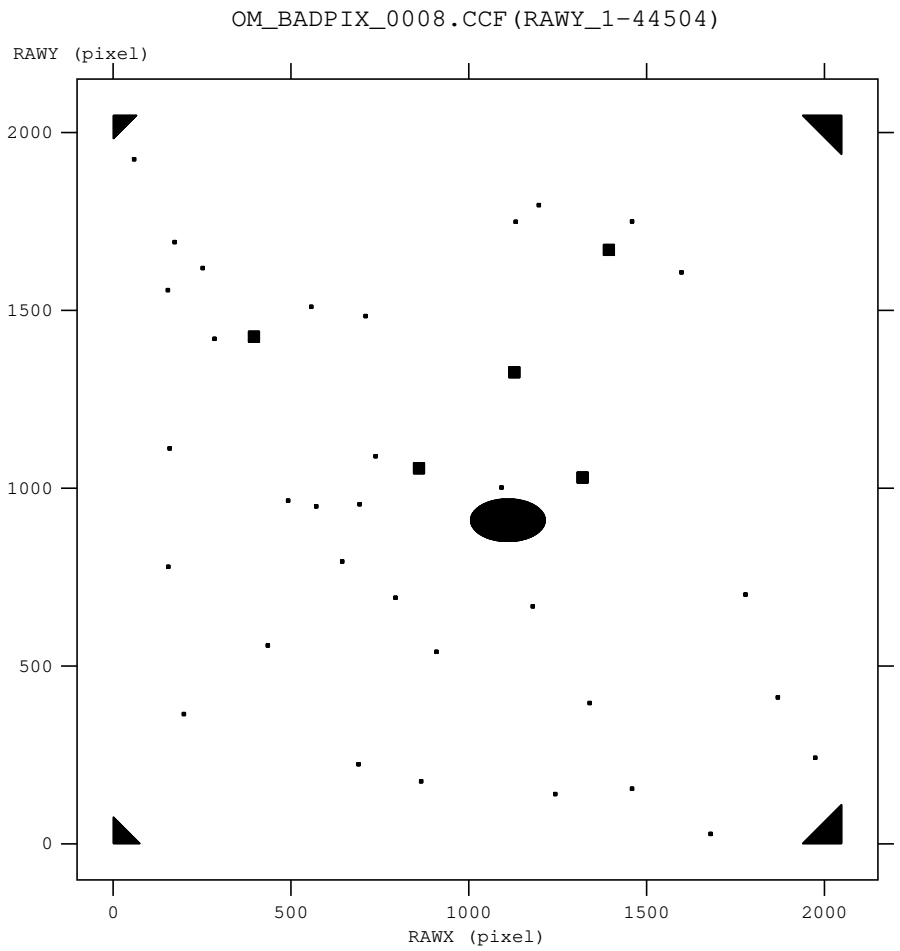


Figure 5: Distribution of bad pixels and low sensitivity areas in the OM detector

Table 1: OM bad pixel coordinates

X	Y	Description	Size (sub-pixel)
396	1426	low sensitivity patch	31 x 31
860	1056		
1128	1326		
1320	1030		
1394	1670		
159	1112	dead pixel	9 x 9
199	365		
866	176		
1680	28		
1869	412		
909	540	hot pixel	9 x 9
1180	668		
1340	396		
1459	155		
59	1925	low sensitivity pixel	9 x 9
154	1557		
155	779		
173	1692		
252	1619		
285	1420		
435	558		
492	965		
557	1510		
571	949		
644	794		
690	224		
693	955		
710	1484		
738	1090		
794	692		
1092.	1002		
1132	1749		
1197	1796		
1243	140		
1459	1750		
1598	1607		
1974	242		
1778	701		
1110	910	Jupiter low sensitivity patch	208 x 118

2.4 Operational modes, source detection and count rate

The Optical Monitor has two basic operational modes known as "image mode" and "fast mode" which can be used simultaneously or not.
OM image mode science data are provided as "images", i.e. bi-dimensional arrays in which the X & Y coordinates correspond to pixel position in the detector (sub-pixels as defined in Section 2.3) and the value or counts is the number of events registered in the pixel.
In fast mode the science data come as a list of events, namely photon detections defined by their arrival times and the pixel positions (X & Y coordinates) in the detector. Fast mode data can be integrated in time to obtain an images of the area where they are recorded.
In both modes, since the detector is a photon counting device, the intensity of the source is given by the count rate rather than the total number of detected events.
Measuring the photon energy coming from the possible different sources in the OM field of view first requires identification of the sources in the image or the event list. Due to the effect of the PSF (see Section 2.6) the size of the source will be of several pixels, whose counts have to be added up to compute the count rate of the source. After finding the sources, their count rates in OM are determined by aperture photometry. A circular aperture of 12 sub-pixels radii (circa 6 arcsecs on the sky) is usually adopted for the U, B and V filters. For the UV filters the aperture has 35 sub-pixels radii (17.5 arcsecs on the sky). When a source is found the total number of counts in the aperture is computed. Then an annular region around the aperture is used to compute the background. The knowledge of the PSF allows us to measure properly the source count rate, even in case of crowded fields. All this is accounted for in SAS.
It is worth noting that the calibration of OM is related to the way in which the count rate of the sources is measured. Using different methods or even different aperture sizes may have an impact on some of the corrections described here and on the calibration parameters.

2.5 Coincidence Loss

The loss of counts through coincidence occurs whenever more than one photon arrives at the CCD in the same place within the same frame. For the 20th magnitude stars, OM coincidence losses are negligible. Losses become significant for a point source at a count rate of about 10 counts/s (about 10% coincidence). Coincidence losses for point sources can be measured empirically if one observes the same stars with the OM as well as from the ground. In this way, one can obtain the coincidence loss fraction

$$F(R_{raw} \times t_f) = \frac{R_{raw}}{R_{true} \times (1 - d_f)} \quad (1)$$

where R_{raw} is the count rate measured by OM, R_{true} is the true count rate from the ground-based observations, t_f is the OM CCD frametime and d_f is the ratio of the CCD deadtime to the frametime.
We have compared the OM and ground measurements of ~ 400 stars to derive an empirical correction to this coincidence loss. Figure 6 shows the theoretical (red line) and empirical (blue line) coincidence loss correction curves superposed on flight data.

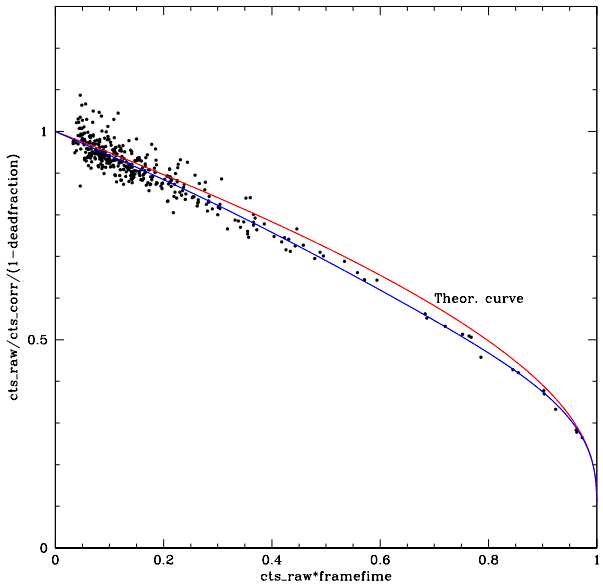


Figure 6: Theoretical (red line) and empirical (blue line) coincidence loss correction curves superposed on flight data.

As the empirical curve is not very much different from the theoretical one, it is reasonable to fit not F itself but the ratio of the empirical curve to the theoretical one. Thus, the empirical coincidence loss correction will have the form

$$R_{corr} = -\frac{\ln(1 - R_{raw} \times t_f)}{t_f \times (1 - d_f)} f(R_{raw} \times t_f) \tag{2}$$

where the best polynomial fit for $f(x)$ $(0 \leq x \leq 1)$ is

$$f(x) = 1.0 + 0.076 \times x - 0.144 \times x^2 + 0.638 \times x^3 - 0.570 \times x^4 \tag{3}$$

Note that the coefficients are $a_0 = 1.0$, $a_1 = -\sum_{n=2}^{4} a_n$, which follows from the adopted condition that $f(0) = f(1) = 1.0$.
This empirical correction has been incorporated into the SAS.

2.6 Point Spread Function

The OM point spread function (PSF) was measured in detail in the early phases of the operational life of the instrument. It is radially symmetric in shape, and its width depends slightly on the brightness of the source. Average FWHM values are 1.35", 1.39", 1.55", 2.0", 1.8" and 1.98" for V, B, U, UVW1, UVM2, UVW2, respectively (see Figure 7).
Since an analytical fit was very difficult, especially in the wings, we have measured the PSF using the method of the curve of growth (percentage of counts contained within a certain radius). The difficulty of this method is to find a number of stars of different brightness spread over the field of view, and sufficiently isolated. Using Daophot in our PSF analysis, we have derived for each filter, a set of PSFs dependent on count to framerate ratios (CFRR), a way of measuring the brightness. The PSF is incorporated into the SAS, through the corresponding CCF.

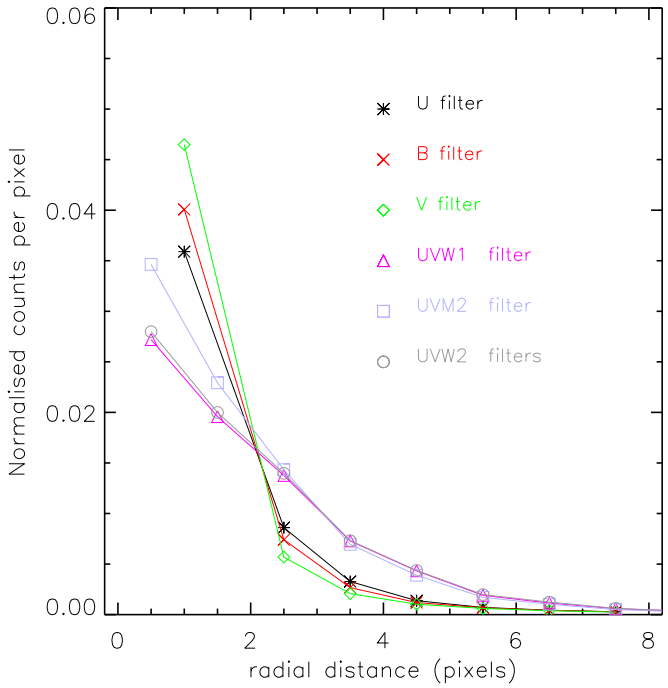


Figure 7: OM PSF in different filters average for different CFRR, the pixel scale is 0.4765" on the sky.

Some operating modes of OM allow the user to bin the obtained images (or observing science windows in the detector) normally 2×2 in X and Y. This produces a slight degradation of the PSF, as can be seen in Figure 8.
The photometry performed with SAS on OM images gives, as a by-product, the FWHM of the detected sources in the field of view. These results have been used to draw the above mentioned Figure 8. They illustrate, as well, the stability of the PSF over the life time of the mission, as shown in Figure 9 where two different OM pointings performed with five years interval are compared. Extended objects present in these figures are clearly identified since they deviate from the linear trend.

2.7 Distortion

The OM telescope optics, the filters and the detector itself, all contribute to a certain amount of distortion in the final image. At the edges of the field of view, shifts of up to 20" are seen (see Figure 10). The distortion map for the U filter has been derived by comparing the actual and predicted positions of 813 stars in the OM calibration field of G153.
The map can be used to correct position to a level of about 0.7 arcsecs RMS error.
Analysis has shown that the offsets between source position measured in the different filters are reduced when applying the U filter based distortion map to all filters. This is not surprising, since the main components of the distortion are due to the photocathode and to the fibre taper that are part of the detector and therefore they are filter independent. This distortion map is used in the SAS for all filters. We should point out that the

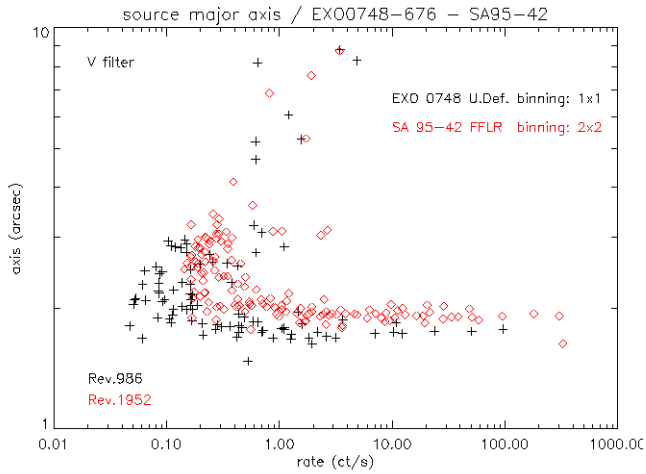


Figure 8: Effect of binning in the OM PSF

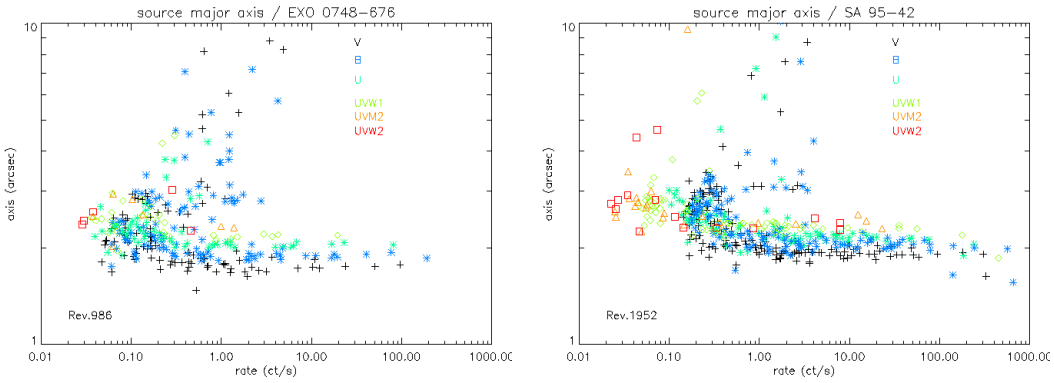


Figure 9: The OM PSF at two different epochs

source positions determined by SAS are based on the satellite attitude information and, therefore, can be a few arcsecs offset from the real positions due to the spacecraft pointing error.

The SAS allows the user to perform a cross-correlation with an existing catalogue (e.g. USNO) to further reduce the astrometric uncertainties. Table 2 gives statistical results obtained on more than two thousand observations processed with SAS.

When using the grisms, there is an additional distortion accompanied by a translation of the zero orders with respect to the position in the direct image.

Observations of the Sco X-1 field with the V filter and both grisms have been used to derive a polynomial fit to this combination of distortion and translation. This allows us to map the positions of the observed zero orders with respect to the direct image and therefore to compute the coordinates of the sources corresponding to the observed spectra. This is important in the case of field spectroscopy when, by using the OM detector in full frame configuration, the spectra of all sources in the field of view are registered. The accuracy of the obtained coordinates is better than 20 arcsecs RMS.

The geometric distortion correction for images obtained with the filters, as well as the additional one affecting the grisms have been included in the OM_ASTROMET CCF.

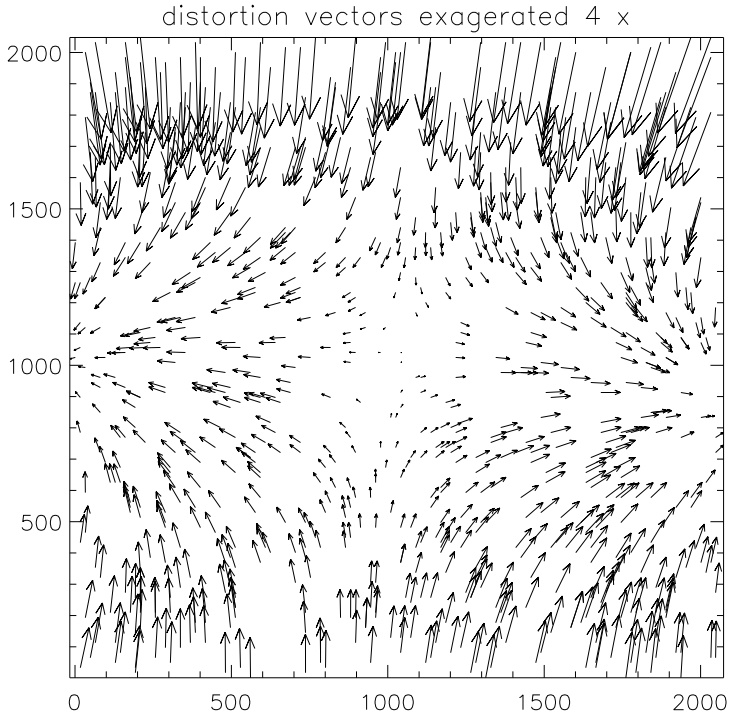


Figure 10: This is a 5th order polynomial fit to the distortion measured from star positions, exaggerated 4 times.

Table 2: Astrometric accuracy obtained with SAS

	mean offset (arcsec)	standard deviation (arcsec)
Right Ascension	-0.36	1.5
Declination	0.54	1.6

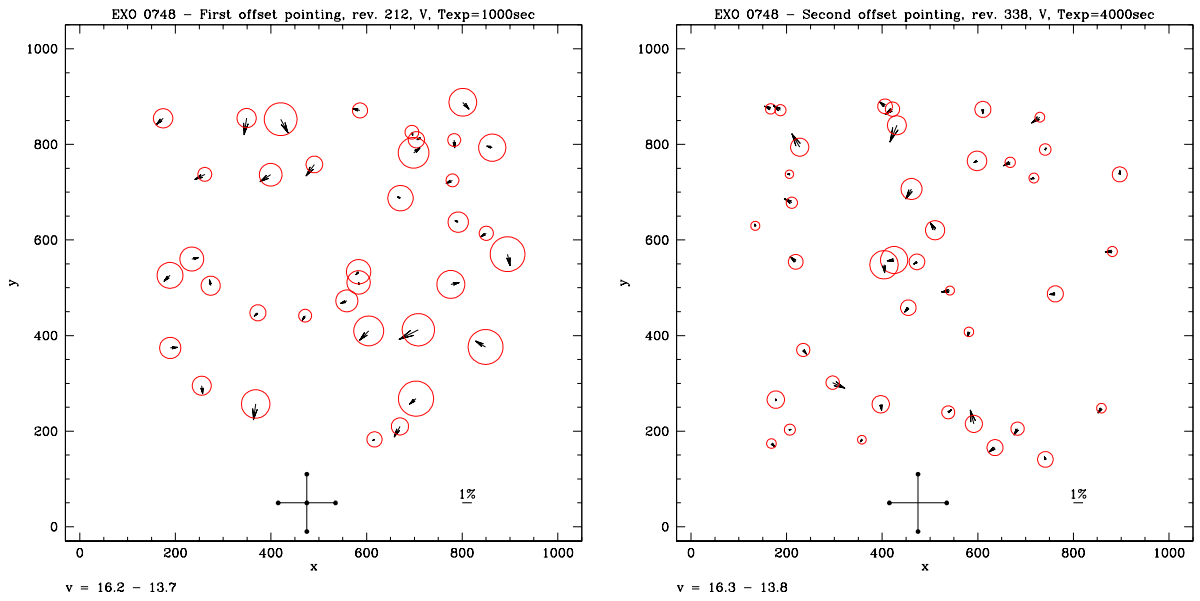


Figure 11: Local gradients vs. Statistical noise. Left: rev. 212, right: rev 338. The crosses show the scale of the offset pointings. The radii of the red circles reflect the statistical uncertainty on the count rate differences at each point while the arrows indicate the magnitude and direction of the mean difference of the 4 offsets pointings from the central one.

2.8 Large scale Sensitivity variation

The first search for possible large scale sensitivity variations was based on two sets of offset observations of the field EXO 0748-67 in V filter obtained in rev. 212 and rev. 338. In addition to the central pointing, there were 4 additional pointings shifted to the North, South, East and West by 2 arcmins. In the first observations the exposure time for each pointing was 1000 seconds, and in the second set it was 4000 seconds. These data allowed us to measure local sensitivity gradients and combine them together to obtain a CCD sensitivity map. Five measurements for every star were used to determine the local gradients, whose values and directions are shown in Figure 11 as arrows. Circle radii reflect the value of the statistical error for each star. If the local gradient is larger than the statistical error, the arrow must be longer than the radius of the corresponding circle. Even if the local gradients are smaller than Poisson errors but systematic, we would see similar orientation of arrows in some areas of the plot. This is not the case, the directions of the arrows seem to be chaotic. Also, if one compares the directions of the gradients in the same areas of the CCD in two observations, one finds no similarity. These results tell us that large scale sensitivity variations, if present, are smaller than the current photometric accuracy of observations and do not exceed a few per cent.
Another way of looking at these data is presented in Figure 12 where the observed count differences for every star measured in different (offset) exposures are compared with the statistical noise of the stellar count rate. The data in this figure were obtained in Rev. 854 following the procedure used in Rev. 338 with similar offset pointings in the field of EXO 0748-67. The plot shows the inter-comparison of different exposures and the fact that the distribution of points follows the line (0,0-1,1) indicates that any large scale variation is

Table 3: OM observations of SA95-42

Rev.	Obs. Id	R.A. (*hours*)	Dec. (*degrees*)	Pos. angle (*degrees*)	Prime	Date Obs	Filters
407	0154150201	3.8955555	-0.075833	261.8	OM	2002-02-27	VBUL S
759	0134921001	3.8954638	-0.075833	251.9	OM	2004-01-31	V ULMS
1051	0134921101	3.8954638	-0.075833	82.9	OM	2005-09-05	VBULMS G1G2
1227	0410780201	3.8954638	-0.075833	76.7	R1	2006-08-22	VBULMS
1408	0410780401	3.8954638	-0.075833	75.3	R1	2007-08-18	VBULMS
1587	0410780601	3.8954638	-0.075833	72.6	R1	2008-08-09	BULMS
1775	0134921201	3.8954639	-0.075833	80.0	OM	2009-08-18	VBULMS G1G2
1952	0410780701	3.8954639	-0.075833	71.7	R1	2010-08-07	VBULMS
Note 1	Prime pos: OM=(1024, 1024), R1=(1091, 975)						
Note 2	Filters: V, B, U, L(UVW1), M(UVM2), S(UVW2), G1(grism UV), G2(grism V)						

of the order of the statistical noise.
Confirming the absence of large scale sensitivity variations during the full life of the instrument, as was done before, requires setting up observations that consume a lot of observing time. However, the same goal can be achieved if we compare observations of the same field at different epochs, obtained with different position angles and different boresights (provided by the choice of different prime instrument). In this way we test possible variations due to both, large scale sensitivity variations and time. We have selected several observations of the standard calibration field SA95-42 and again some more data of EXO 0748-67 obtained from the XSA.
Table 3 and Table 4 give the observations of the SA 95-42 and EXO 0748-67 fields, used to extend the study of large scale sensitivity variations. In particular, the use of observations obtained with very different position angles allows us to study variations over larger scales than the ones obtained by offset pointings.
In Figure 13 we show the comparison of observations of SA95-42 with combinations of different position angles and offsets obtained regularly between Revs. 407 and 1587. The results shown in Figure 12 are confirmed here.
More recent confirmation is shown in Figure 14, where three sets of observations of both EXO 0748-67 and SA95-42 are compared in the same way. The fact that the comparison shows that the differences in count rates of all stars are of the same order than the statistical error, confirms the validity of the time sensitivity correction and that large scale variations are of the same order as the errors of the photometry.
The SAS assumes no large scale sensitivity variation and this should not degrade the accuracy of the OM data.
Breeveld et al (2010), have found sensitivity variations of up to 9% on very large scales (8-10 arcmins) in the UVOT on board SWIFT. The UVOT has a very similar detector to OM, therefore their finding suggests that the same might occur in OM. It is a goal to extend the analysis for the OM, using more fields and the same techniques described before, to more tightly quantify any such variations in our instrument.

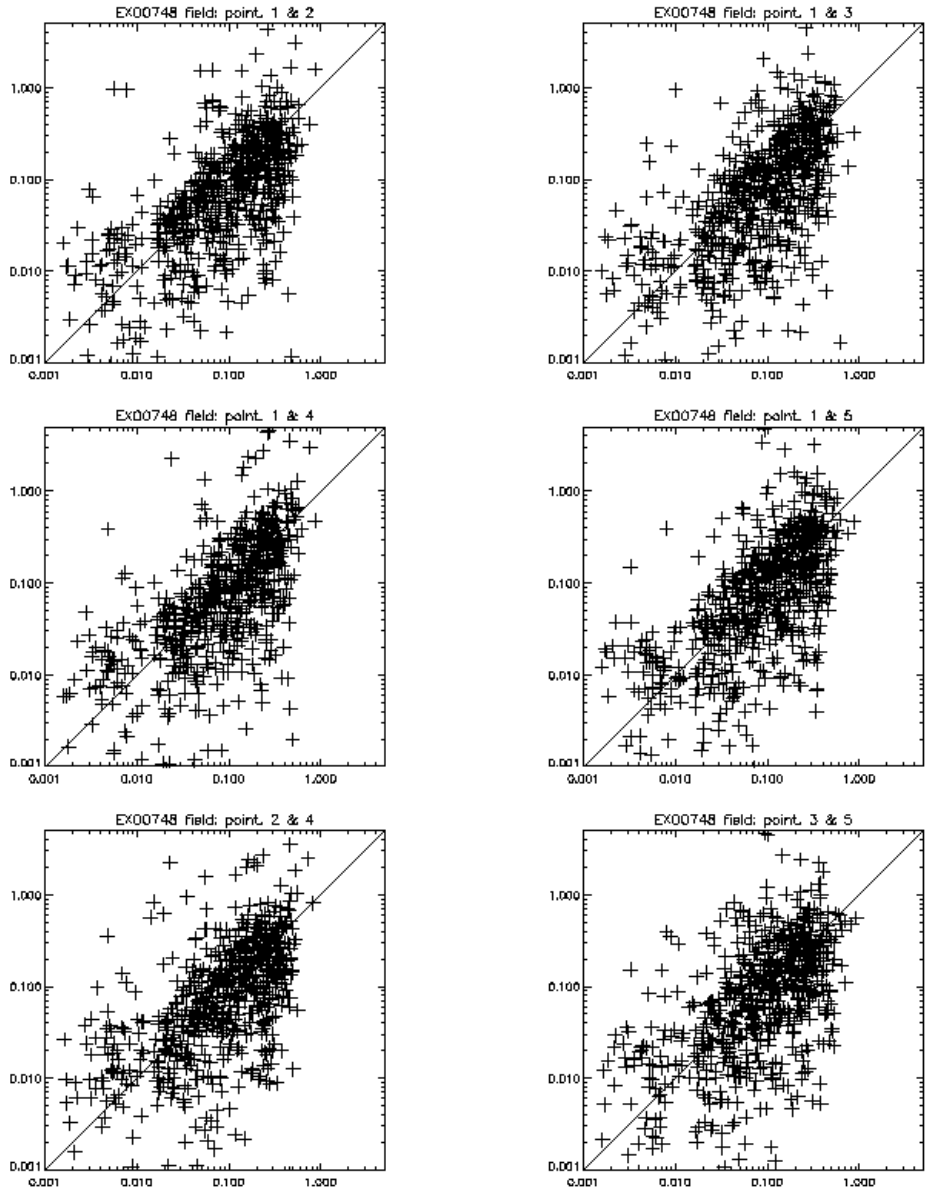


Figure 12: Observed count rate differences in the offset observations of the EXO 0748-67 field versus statistical noise. Filter V. Revolution 854.

Table 4: OM observations of EXO 0748-67

Rev.	Obs. Id	R.A. (*hours*)	Dec. (*degrees*)	Pos. angle (*degrees*)	Filters	Position
212	0134561201	7.807	-67.75	200.1	V	onaxis
212	0134561401	7.807	-67.78	200.1	V	off3
212	0134561501	7.813	-67.75	200.0	V	off4
212	0134561301	7.801	-67.75	200.2	V	off2
212	0134561101	7.807	-67.71	200.1	V	off1
338	0134562401	7.809	-67.79	83.3	V	off3
338	0134562501	7.815	-67.75	83.2	V	off4
338	0134562201	7.809	-67.72	83.3	V	off1
338	0134562301	7.804	-67.75	83.4	V	off2
338	0134562101	7.809	-67.75	83.3	V	onaxis
854	0134562801	7.809	-67.72	20.2	V	off1
854	0134562901	7.803	-67.75	20.3	V	off2
854	0134563001	7.809	-67.79	20.2	V	off3
854	0134563101	7.815	-67.75	20.2	V	off4
854	0134562701	7.809	-67.75	20.2	V	onaxis
986	0212480501	7.809	-67.75	281.9	VBULMS	onaxis
1698	0605560401	7.809	-67.75	240.6	U	onaxis
1927	0651690101	7.809	-67.75	330.0	U	onaxis
Note 1	Filters: V, B, U, L(UVW1), M(UVM2), S(UVW2)					

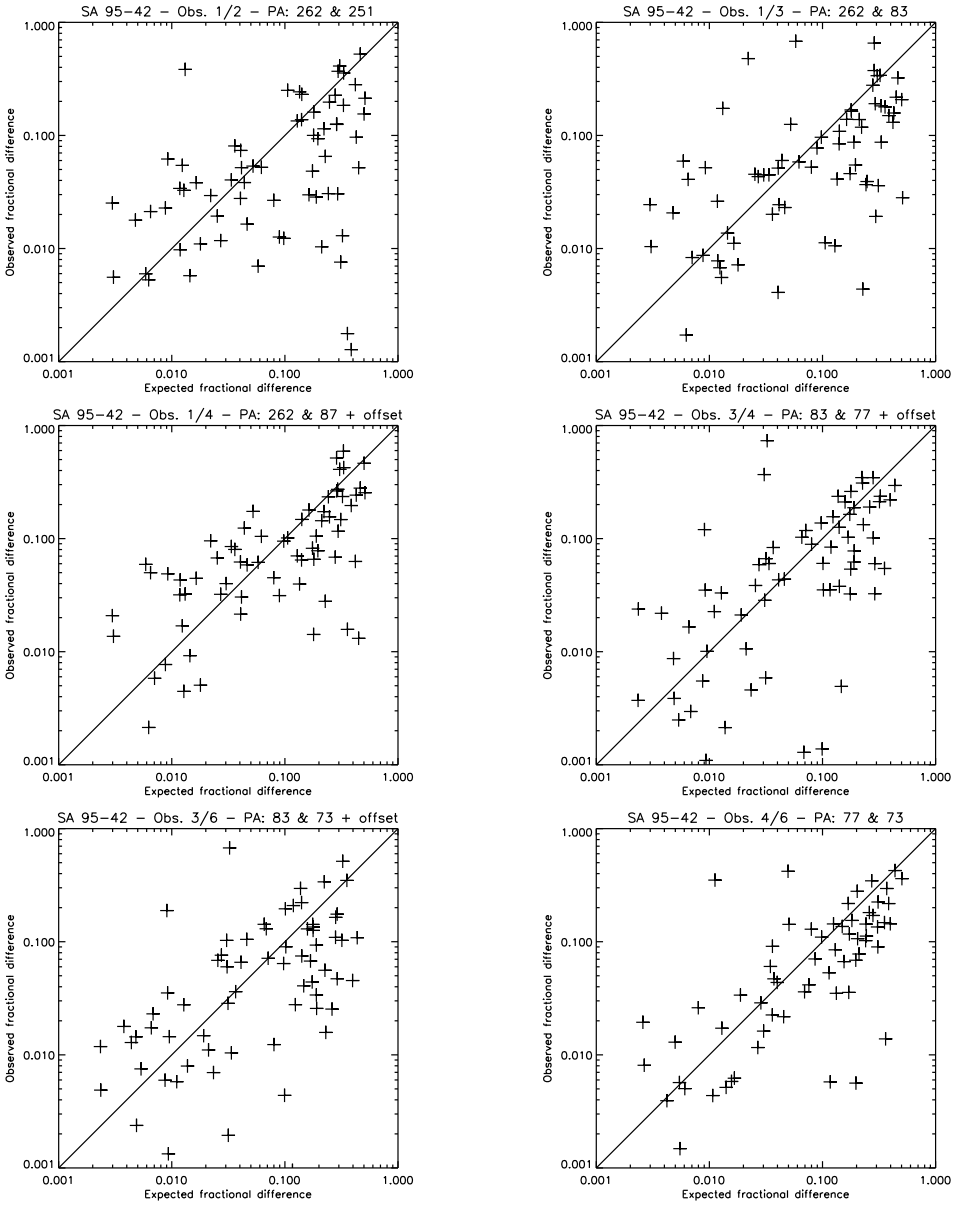


Figure 13: Observed count rate differences in observations of the SA95-42 field versus statistical noise.

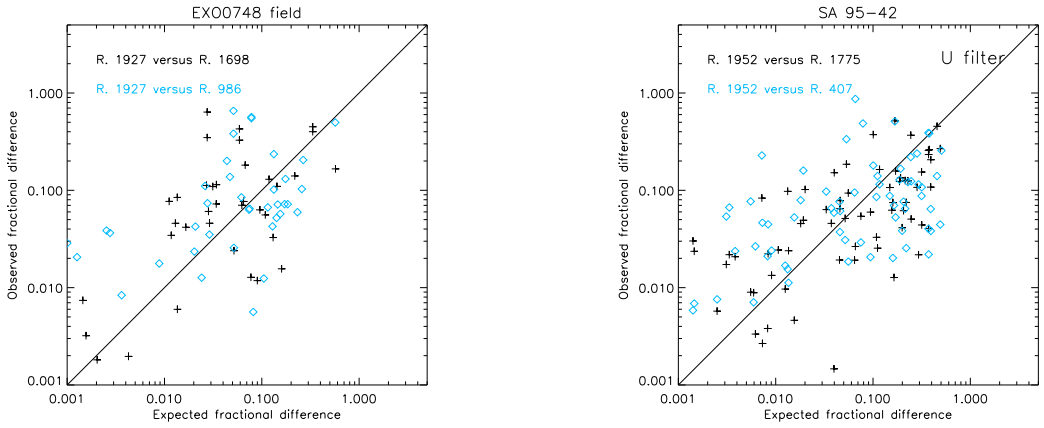


Figure 14: Observed count rate differences versus statistical noise in observations of EXO 0748-67 and SA95-42.

Table 5: Levels of different OM background contributors.

Background source	**Occurrence**	**Count rate range**
Diffuse Galactic[1,2]	all directions	0.214–7.968×10^{-6}
Zodiacal[1,2]	longitude 90° ± 20°	0.169–5.611×10^{-6}
Average dark count rate[1,3]	all directions	1.02×10^{-3}–1.60×10^{-3}
Note 1	rates in unit $cts/s/arcsec^2$	
Note 2	maximum in White filter	minimum in UVW2
Note 3	dark count rate increased after rev.800	

2.9 Background

The sources of background illumination in OM are zodiacal light, diffuse galactic light and internal noise (dark current). The zodiacal light dominates the background in the optical, while in the bluest UV filters the intrinsic detector background becomes important.
A detailed study of the OM background can be found in Poole (2006). A summary is given in Table 5.
The mean sky background count rate has been estimated in each of more than 58000 OM images, after excluding pixels with flagged quality issues and statistically clipping brighter outlier pixels from the images. The average background count rate values for all OM filters for revolutions between 500 and rev 3657 are given in Table 6. In the UVM2 and UVW2 filters (and, to a much lesser extent, the UVW1 filter), the background shows a prominent variation with time, which closely follows the variation of the dark count rate (see section 2.1), which indicates the dark count rate represents a substantial component of the background level in these filters.

Table 6: The background count rate in unit $cts/s/arcsec^2$

Filters	V	B	U	UVW1	UVM2	UVW2	V Grism	UV Grism	White
	0.0209	0.0325	0.0131	0.0042	0.0019	0.0016	0.1217	0.1064	0.0691

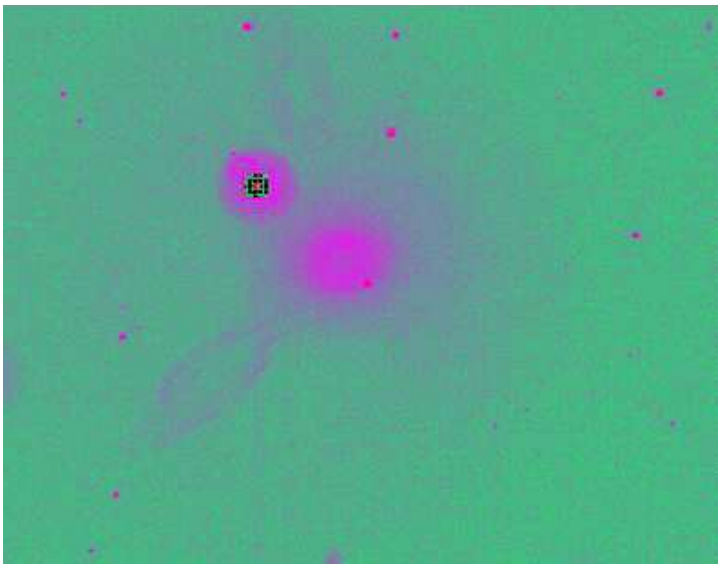


Figure 15: This image of the SA95 field in the B filter highlights three scattered light features seen in OM images: (i) an out-of-focus ghost image ("smoke ring") of the bright star, caused by an internal reflection of the star light from the detector window, can be seen, radially displaced to the upper left of the bright star, within its PSF halo; (ii) extended elliptical loops caused by scattering of light of bright, off-axis (12.1'-13') field stars by the detector housing; (iii) a central, diffuse doughnut due to off-axis background light scattering off the detector housing.

2.10 Straylight

There are two causes for the straylight appearing in the OM images. First, there is an internal reflection of light within the detector window, which produces an out-of-focus ring ("smoke ring") image of a bright star displaced in the radial direction away from the primary image. The second effect is due to the reflection from part of the detector housing, of off-axis starlight and sky background lying between 12.1 and 13 arcmins from the center of the field of view. The reflected star light causes low-intensity loops and streaks in the image, while the reflected background produces a diffuse annular pattern in the center of the image. Besides these two well-known straylight features, we also find a few small features in the corners of the images which could be mistaken for real sources. Since SAS uses aperture photometry to measure the source flux or magnitude, straylight only increases the local background, thus reducing the sensitivity, but it does not affect source detection and magnitude too much. This can be seen from Figure 15 which is an OM observation of the SA95-42 field in the B filter. The standard star (SA95-42) at the center is just in the position of the bright straylight ring. Stetson (Stetson, 2000) found its standard V and B magnitudes are 15.606 and 15.392, and we obtain V=15.62 and B=15.50 from OM observations.

2.11 Fixed patterning

Fixed patterning (also known as modulo_8 noise) is a side effect of the centroiding of the photon splash on the CCD resulting from one photon incident on the front end of the detector. As explained in Section 2.3, by centroiding, the 256 × 256 real CCD pixels

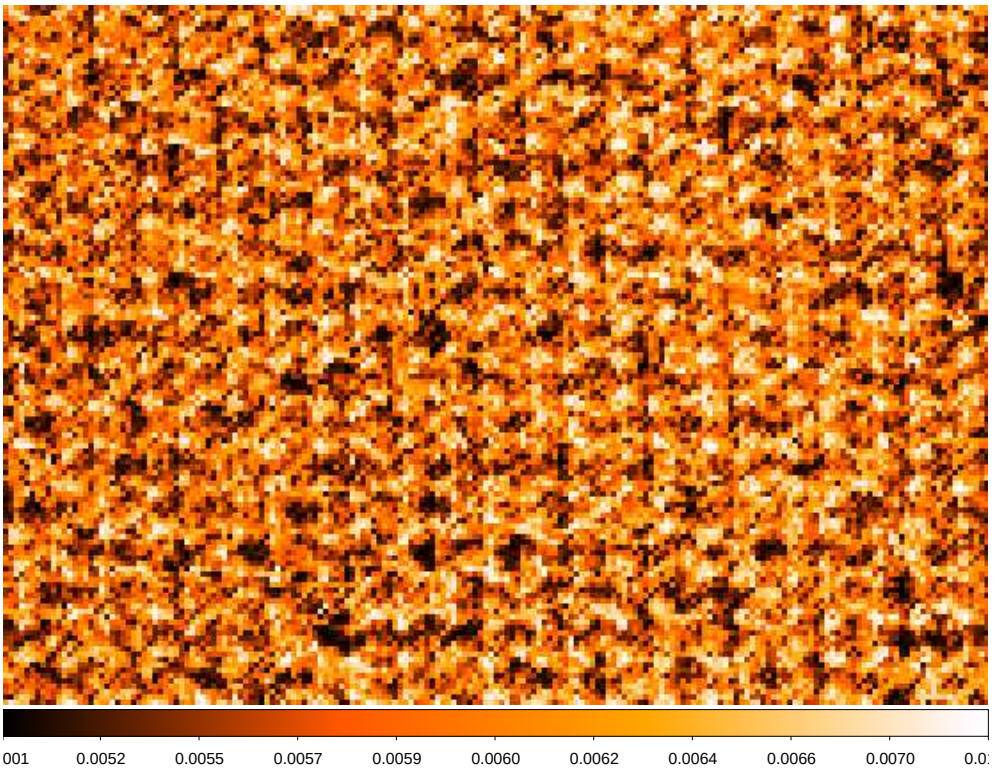


Figure 16: A portion of a flatfield image that highlights the regular (8-pixel) modulo-8 fixed patterning effect that arises from the imperfect onboard event centroiding process

.

are "converted" into 8 x 8 sub-pixels, giving a 2048 × 2048 final frame. The centroiding algorithm, applied in real time, produces "pixels of unequal sizes". To correct for this effect, we use a lookup table that cannot take into account variations in photon splash shape over the surface of the detector, thus producing a pattern that repeats on an 8 × 8 sub-pixel grid - an example of the effect is shown in figure 16. However, the average modulo 8 noise can be measured from the background sky, and then the counts may be re-sampled based on the true pixel sizes, as is done in the SAS modulo-8 correction routine. This is possible where there are sufficient counts to determine the resampling but in some cases, more typically affecting UV exposures, the statistics are insufficient and the modulo-8 correction cannot be performed.

3 OM simulations, Throughput, Effective Area and Zero-points

3.1 In-flight throughput and time sensitivity degradation

The photometric throughput of the OM has been monitored regularly throughout the mission (the throughput of the grisms is discussed in section 7.3). Initially, this was achieved via systematic observations of standard stars, whose spectral energy distributions are well known. However, from 2017 until April 2024, the analysis was instead based on use of a subset of stars extracted from the OM Serendipitous Ultraviolet Source Survey (SUSS) catalogues (Page et al., 2012), each of whose light curves comprised at least

Table 7: Parameters of the new exponential sensitivity degradation model, for each OM filter. As the reference epoch, $t_0(MJD) = 51544.0$, is fixed and is the same for all 3 stars and all filters, it is not included in the table

filter	f	t_d (days)
V	0.1388	1655
B	0.1097	3943
U	0.1133	4101
UVW1	0.1442	3119
UVM2	0.2402	2624
UVW2	0.2267	2393

6 observations and whose count rates, corrected for the degradation determined in the previous analysis cycle, were deemed 'constant'. Normalising the count rate of each star (separately in each filter), by its mean corrected rate (effectively the observed rate at the start of the mission), enabled the timeseries of all such sources to be overlayed in time, confirming the decaying sensitivity trend and, via polynomial fits to the decay trend, enabling the decline (and its correction) in each wavelength band to be quantified. This decay is most likely due to aging of the detector, in particular of its S-20 photocathode, and the effects of contamination from the outset of the mission.
However, in 2024, it was decided to return to the use of the standard stars, principally because these sources are known to be constant; the catalogue based approach is dominated by fainter sources (with large scatter) and the method is reliant on previous corrections for the normlisations, which can bias the sample used in subsequent analyses. The revised analysis, based on the standard stars, is however, modified compared to the earlier standards-based approach: given that, in all filters, the decay has flattened and appears to be approaching a constant value, the uncorrected data from each of the 3 standard stars (the white dwarfs, BPM16274, Hz2 and GD153) have been fitted simultaneously with an exponential model of the form, $R_s(t) = R_s(t_0)[f.e^{-(t-t_0)/t_d} + (1-f)]$, where $R_s(t)$ and $R_s(t_0)$ are the source count rates of standard star, s, at time (MJD), t, and at t_0 (the start of the mission, taken as MJD 51544.0), respectively, t_d is the decay constant of the exponential (in days) and f is the fraction of the initial count rate that is subject to decline; $(1-f)$ is the asymptotic (residual) constant level. In the fitting process, the values of f and t_d are common to all 3 sources but each has its own fitted normalisation, $R_s(t_0)$. In this way, the results do not depend on the previous correction to determine the normalising factors - they are derived via the fit. Due to the additional sensitivity degradation arising at the pn boresight, which lies in the wings of the Jupiter patch (see 2.2.1), the analysis used measurements of the standard stars at the OM and pn boresight positions prior to revolution 3224 and from locations offset from the Jupiter patch after rev 3224. In table 7, we present the parameters of the simultaneous exponential fits to the measured data of the 3 standard stars, for each filter.
In figure 17, panels are shown for each filter, containing the normalised standard star data. The best fit exponential model (black) is compared to the previous polynomial fits (orange) to the SUSS4 catalogue data. It is evident that in the V and UVW2 filters, there

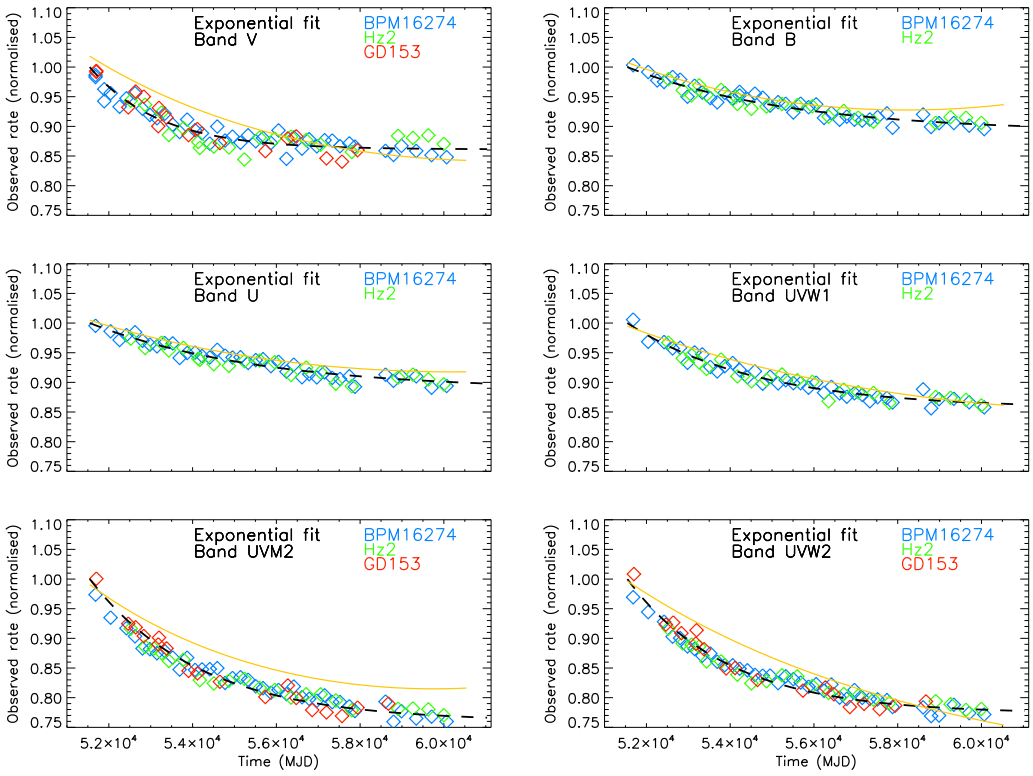


Figure 17: The normalized count rates of the standard stars, BPM16274 (blue), Hz2 (green) and GD153 (red), as a function of time. Each panel is for a different filter, as indicated in the panel. The GD153 data is not included for B, U and UVW1 bands because it is bright in these bands and has a high coincidence loss correction. The black dashed curves are the best fitting exponential models to the data while the orange curves are the previous polynomial fits based on the SUSS4 catalogue data.

are discrepancies of up to 4% at some epochs (especially from MJD ∼53000 - 55000, while for UVM2, the fit to the standards is systematically lower than that to the catalogue data by up to 4%. It is recognized that some of this may be due to intrinsic time-dependent spatial sensitivity variations on the detector which are not formally mapped but for which upper limit estimates of few percent (see 2.8) have been derived.
Filter-dependent correction factors (the inverse of the exponential decay value at a given epoch), based on the new exponential characterisation of the degradation, are applied automatically in the XMM OM SAS analysis from SAS 22 (inclusive), to convert the measured rates to corrected measurements at a zero epoch (adopted mission start as January 1 2000 = MJD 51544).

$$Corrected_rate = Measured_rate \times Correction_factor \quad (4)$$

These exponential models replace the previous polynomial-based corrections.
We note that, in addition to the general (exponential) time-dependent sensitivity correction described above, a new, additional correction is applied for sources observed at the pn boresight (generally targets), after revolution 3224, which accounts for the additional degradation there due to the Jupiter patch. This is discussed in section 3.4.

Table 8: OM fudge factors for Zero epoch

filter	UVW2	UVM2	UVW1	U	B	V
fudge factor	0.157	0.259	0.411	0.486	0.511	0.564
error (stdev/mean)	0.062	0.045	0.041	0.039	0.016	0.009

Table 9: Measured count rates (cts/s) versus predictions using the OM effective areas

BPM 16274							
filter	UVW2	UVM2	UVW1	U	B	V	White
predicted rate	14.3	29.2	72.3	109.0	107.0	32.1	481.
observed rate	14.7	30.4	72.9	113.0	107.9	32.6	436.
difference (%)	2.8	4.1	0.8	3.7	0.8	1.6	-9.5

Laboratory measurements of all Optical Monitor components (reflectance of mirrors, transmission of filters, quantum efficiency of detector chain,....) allow us to predict the throughput of the OM system. After launch, the in-flight throughput was found to be lower than expected, in particular in the UV filters.
Once the OM measured count rates are corrected and referred to a zero time epoch, we can define a fudge factor for OM simulations for the zero epoch to account for the deficit of throughput. If we compare the predicted count rates for a series of standard stars we have observed with OM in all filters and we average them, we obtain the fudge factors given in Table 8.
The in-flight throughput deficiency can be explained by molecular contamination of the OM system. Figure 18 taken from Kirsch et al(2005) shows the OM in-flight throughput derived from observations of spectrophotometric standard stars, compared with the predictions obtained by considering several densities of the contaminant material. A density of 30 $\times 10^{-7}$ g/cm^2 can account for the deficit in transmission.

3.2 Effective areas and response matrices

Computing the effective area of the OM system needs to take into account the contribution of all elements, mirrors, filters, detector chain,..., and also the throughput deficiency. The latter is taken into account by fitting a polynomial to the measured fudge factors for each filter. When this is done, and we use the effective area to predict the count rate of the observed standard stars, we need to further adjust the fudge for the UV filters. This is done by an additional factor in the UVW1 and UVM2 filters. The difference with the observations achieved by this final effective area can be seen in Table 9 where we compare the measurements of the standard star BPM 16274 (mean of 19 observations spread over the first half of the life of the instrument) with the predictions obtained using the effective areas.
Figure 19 shows the OM effective area for all filters.

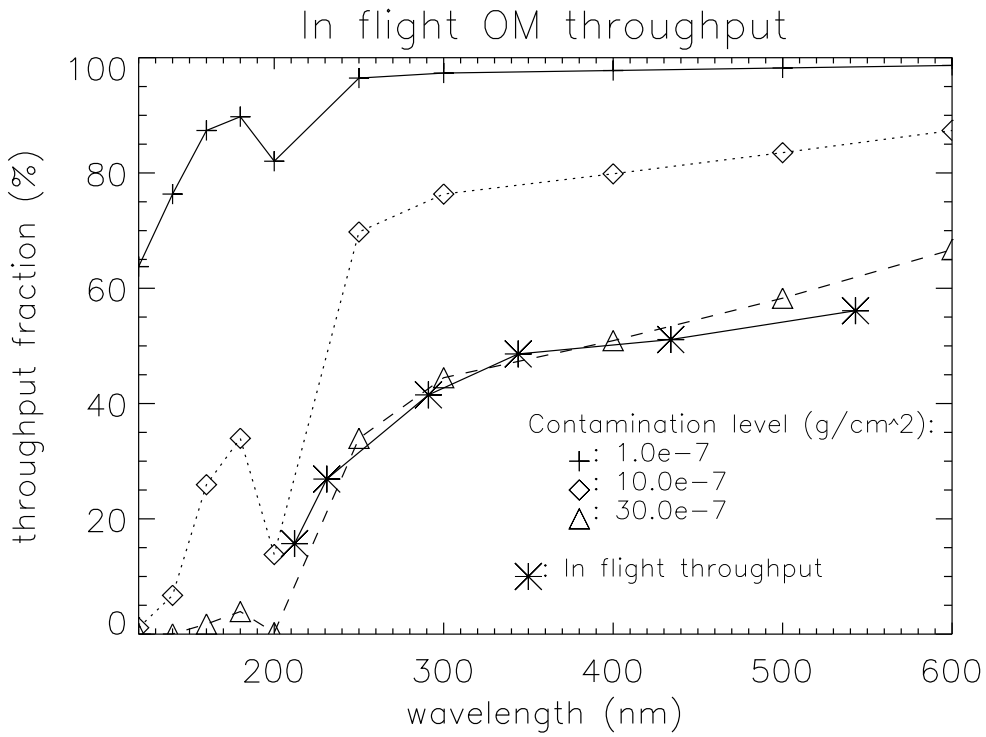


Figure 18: OM throughput with molecular contamination. In flight throughput is represented with stars and a thick line

Response matrices to be used in Xspec type environments have been derived from the effective area.

3.2.1 The White filter.

Since there were no OM observations of our standards with the White filter because of their brightness, we have taken the polynomial fit for the molecular contamination and we have combined it with the laboratory measurements of the filter and all other elements. We have been observing the standard star BPM 16274 with the white filter since Rev.1449. Despite the large coincidence losses (due to the count rate being above 400 c/s) the simulations using the white filter effective area agree with the measured values to within 11% (see Table 9). Since no correction for time dependent sensitivity degradation is applied in the case of the White filter, this difference might be due to the absence of such correction.

3.3 Red leak in UV filters

The OM UV filters (see Fig.20) transmissions have very faint red-ward tails. Even if they are a few orders of magnitude smaller than the filter transmission peak, their contribution to the measured count rate can be significant in the case of very cool objects with little flux in the UV but bright in the visible range, e.g. K or M type stars. Table 10 shows that for a K0V star, the UVW2 counts due to photons of wavelengths beyond 4000 Å

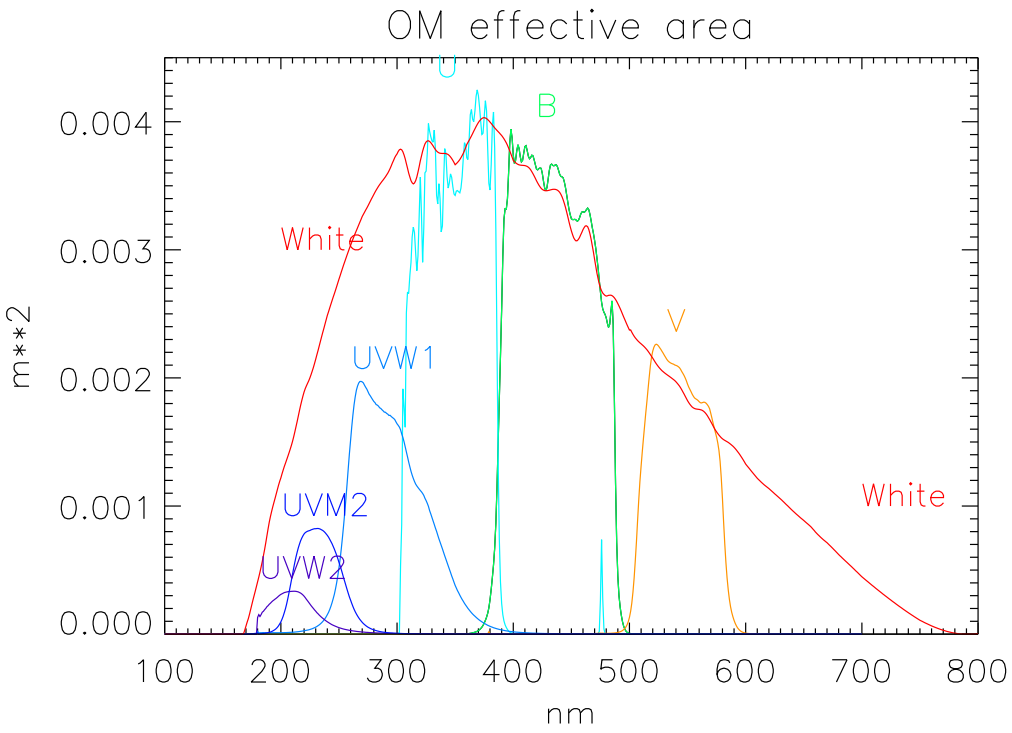


Figure 19: The current optical Monitor effective area curves for each of the filters

can be as high as 29 % and 60 % from beyond 3000 Å.

3.4 Sensitivity impact of the Jupiter patch

As noted in section 2.2.1, the Jupiter observation event (hereafter, JO)) in revolution 3224 led to a substantial degradation of the throughput in a small region near the centre of the OM detector, with the V band being worst affected. Much of the affected region is identified in the bad pixel CCF (section 2.3) but not all. The wings of the patch extend beyond the pixels flagged in the CCF and, in fact, slightly affect the RGS and pn boresight locations (observation targets are generally placed at the pn boresight), thus impacting on their photometry. Sources in the patch are, currently, generally not corrected for this extra degradation in SAS processing (but see below).
Routine monitoring observations of standard stars at the boresight location over the mission baseline (and, since 2019, also at offset locations well outside the patch), provide a measure of the impact of the patch on target sources. In figure 21 we show the timeseries of the standard star, BPM16274, in each filter, corrected for the general OM time-dependent sensitivity degradation (based on the previous OM catalogue based polynomial characterisations of the decline - see section 3.1). Measurements of the star at the boresight location after revolution 3224 (squares) show a significant drop in corrected count rate relative to the unaffected data (diamonds and crosses). As noted in the previous version of this document, it is now clear that this localised extra degradation at the pn boresight shows a broadly linear ongoing decline in most filters, as is evident in figure 21. The degradation at the boresight will continue to be regularly monitored using the standard

Table 10: Visible photons into UV filters

spectral type	filter	% from $\lambda \geq$ 400nm	% from $\lambda \geq$ 300nm
A0V	UVW2	0.46	0.59
	UVM2	0.04	0.34
	UVW1	0.76	
Vega	UVW2	0.42	1.46
	UVM2	0.03	0.31
	UVW1	0.77	
F0V	UVW2	1.57	4.99
	UVM2	0.12	0.88
	UVW1	1.02	
G0V	UVW2	11.4	31.1
	UVM2	0.72	4.19
	UVW1	1.41	
Solar	UVW2	12.5	33.7
	UVM2	0.82	4.68
	UVW1	1.40	
K0V	UVW2	28.7	60.7
	UVM2	2.45	9.22
	UVW1	2.23	

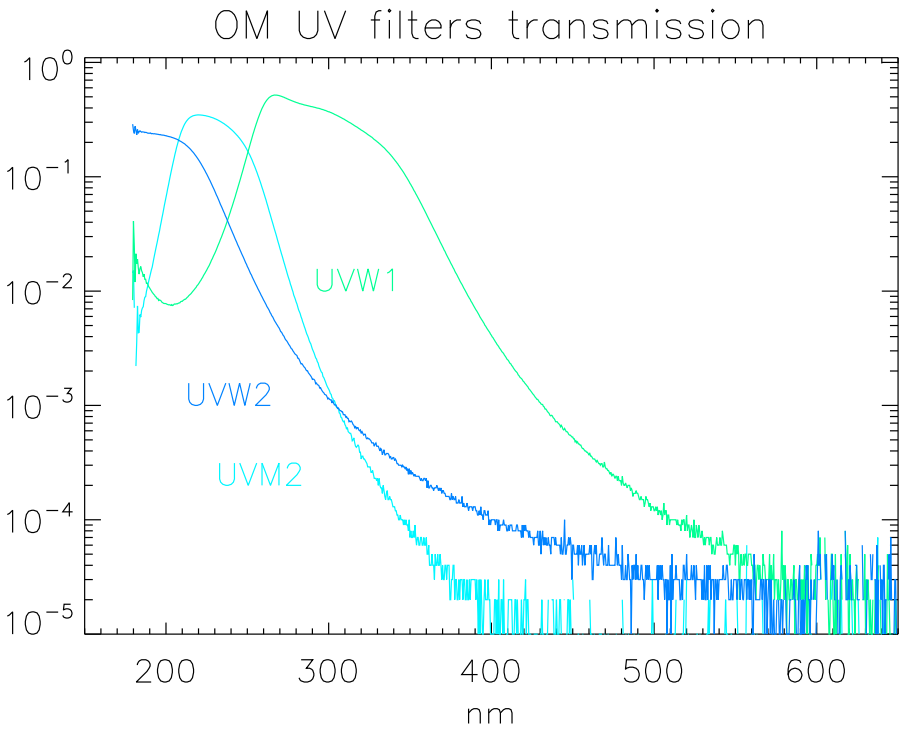


Figure 20: Red-ward tails of the OM UV filters

stars.

The declining trend at the boresight, without the effects of the Jupiter patch, can be inferred from the exponential description of the frequent pre-JO observations of the standard star, BPM16274, and its post-Jupiter-observation data from offset locations outside the Jupiter patch (outlined in section 3.1; see also XMM-CCF-REL-409). In fact, the pre-JO observations of BPM16274 were mostly performed at the OM boresight, which lies about 35 arcsecs away from the pn boresight, but the trend at the OM and pn boresights are essentially consistent within about 1%, based on the data from BPM16274 and from the other standards more frequently observed at the pn boresight. For epochs > revolution 3224, the ratio of the exponential long-term trend (LTT) inferred at the pn boresight, to the linear description of the post-Jupiter observation data from the pn boresight position, gives an approximate correction factor, as a function of time, for the additional sensitivity decline at the pn boresight (an example of the data for the V band of BPM16274 is shown in figure 22). Since the rate of decline in the LTT has slowed markedly, in all filters, the residual inferred throughput is approaching constancy and the LTT/boresight correction ratio is well described by a slowly curving second order polynomial, which is provided in tabular form in the OM_PHOTTONAT_0009.CCF file for revolutions > revolution 3224, being reliable to about 2%. The largest correction is in the V filter, amounting to about 8% at rev 3224 and extrapolating to around 19% at revolution 4700. The tabulated correction values are provided in Appendix E. A more comprehensive discussion of the analysis is given in the CCF release note, XMM-CCF-

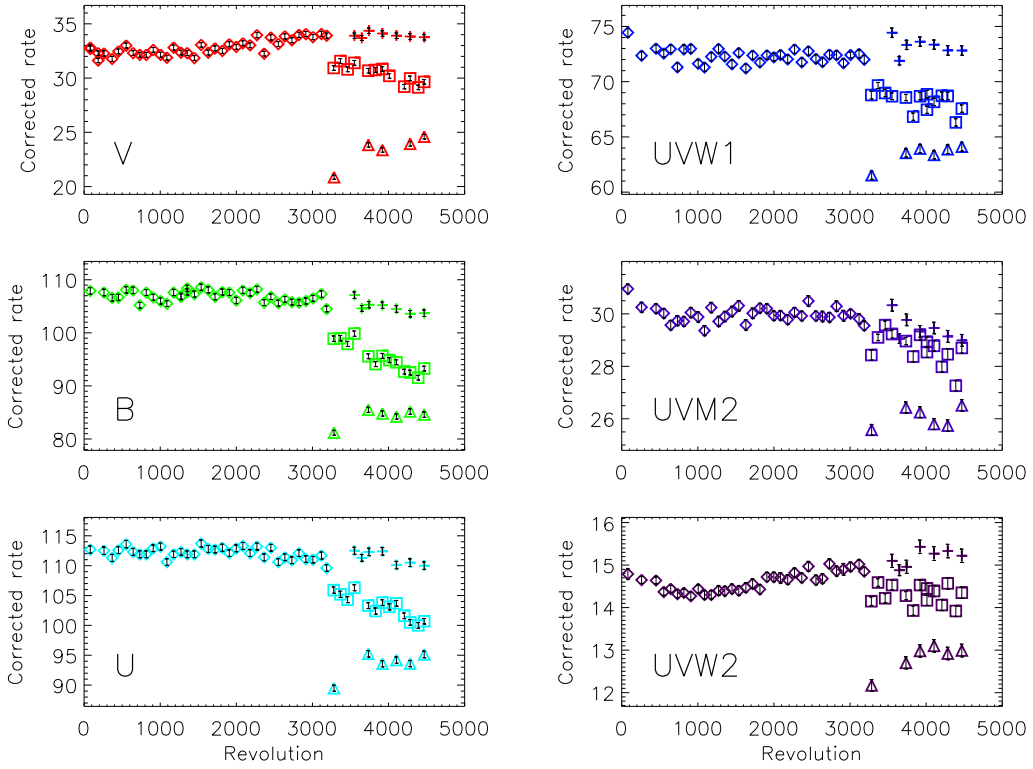


Figure 21: Timeseries of the standard, BPM16274, corrected for the general instrument TDS degradation, for each narrow-band filter, as indicated in the panels. Diamonds and squares represent measurements at the boresight prior to, and after the Jupiter observation, respectively, while crosses are data taken after the Jupiter observation but at locations well outside the patch. Triangles are measurements taken near the core of the patch. The earliest of the observations at the Jupiter patch core was made at a location a few arcseconds displaced from the others, which, given the rapid profile changes near the core, likely mostly explains its lower measured rate compared to the later core measurements

REL-409[1]. This correction is applied automatically from SAS 22 (inclusive) onwards, in addition to the correction for the general OM (exponential) senstivity degradation, but we emphasize that this additonal boresight correction is only applied to sources within 7.5 arcsecs of the pn boresight position: sources at other locations within the Jupiter patch are not corrected (they suffer different levels of sensitivity loss due to the spatial sensitivity profile of the patch).
A full correction for the Jupiter patch is clearly desirable but requires both the creation of filter-dependent flat-field calibration images that fully embed the patch characteristics, and also significant changes to the OM SAS tasks to ensure the statistical properties of source data are correctly propagated. The impact of the Jupiter patch on OM grism data is discussed in section 7.3.1.

[1]https://xmmweb.esac.esa.int/CoCo/CCB/DOC/Attachments/CAL-SRN-0409-1-2.pdf

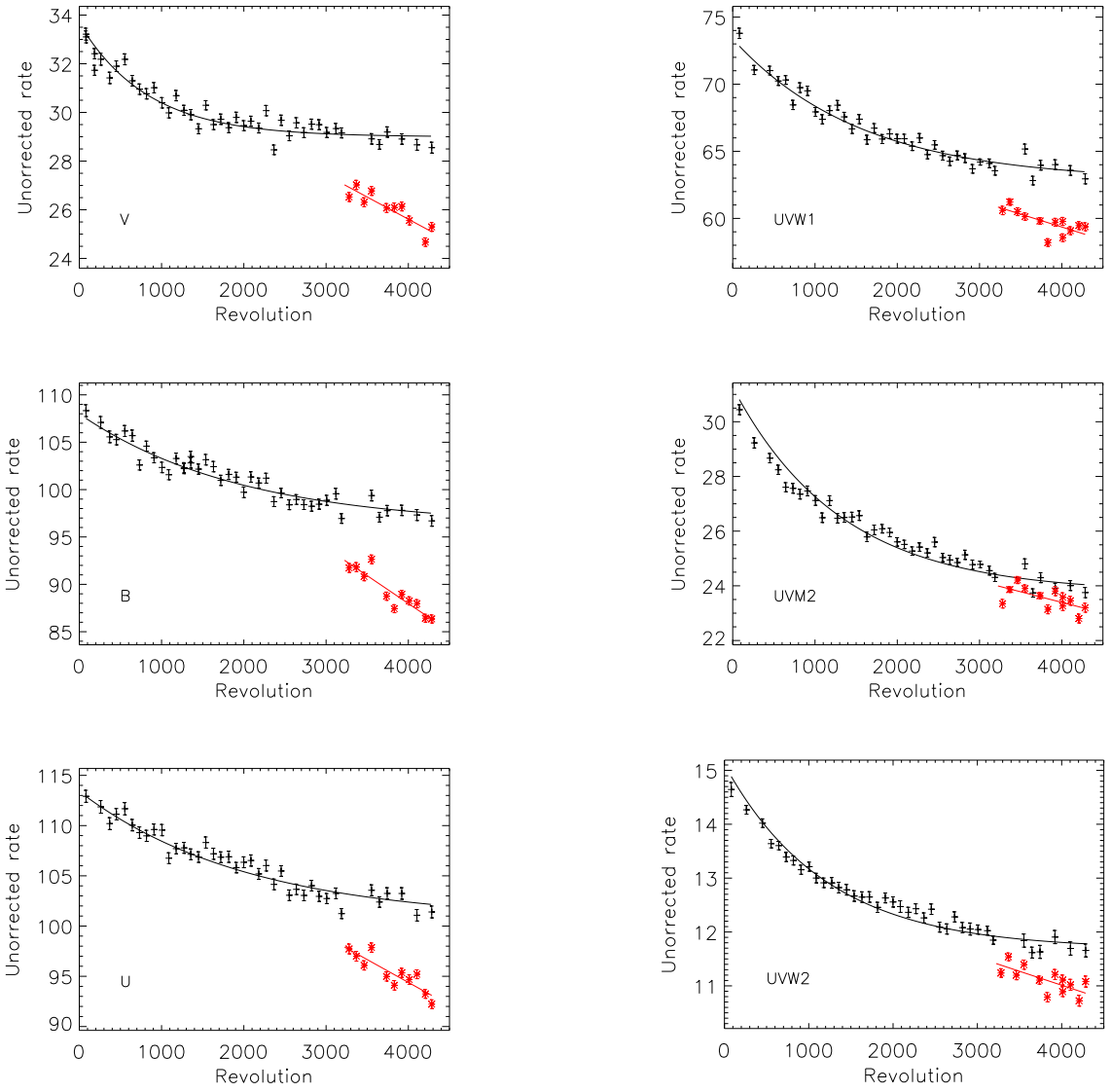


Figure 22: Timeseries of the data in each filter from the standard star, BPM16274, corrected for coincidence loss but not for the general TDS degradation, highlighting the sudden decline in throughput after rev 3224. Data observed at the (mostly OM) boresight prior to rev 3224 and at offset locations thereafter, are shown by black markers. The black curve is the exponential decline function derived from a simultaneous fit to all 3 standard stars (BPM16274, Hz2 and GD153) (see 3.1) routinely used to monitor the OM sensitivity, but with the normalisation relevant to BPM16274. The red points indicate the measurements of BPM16274 made at the pn boresight, after the Jupiter observation, while the red line is the linear fit to them.

Table 11: Zero-points of OM

V	B	U	UVW1	UVM2	UVW2	white
17.9633	19.2661	18.2593	17.2038	15.7724	14.8667	20.2555

4 OM Photometry

4.1 Zero points

In a photometric system for photon counting devices, the Zero point is defined as the magnitude of a source giving one count/sec. The star, Vega, is the primary photometric standard and we use it to define the OM instrumental photometry system. For each filter we can define:

$$Zero_point = 2.5 \times log10(cts_{Vega}) + m_{Vega} \quad (5)$$

where cts_{Vega} is the count rate of Vega in the different OM filters. Since Vega is too bright to be observed with OM we obtain the corresponding count rate from simulations (effective area) as described before.
OM band-passes do not differ significantly from the standard UBV ones. Thus, we have chosen the zero points such that the OM ubv synthetic magnitudes for Vega match the observed UBV magnitudes, respectively. As observed Vega magnitudes we have adopted the values 0.025, 0.03 and 0.03 for U, B and V filters. Since the UV filters do not match any existing photometric system, the zero points can in principle be set to any values. We have chosen $UVW1_{Vega}$=$UVM2_{Vega}$=$UVW2_{Vega}$=0.025.
For Vega simulations we use a spectrum that is the average of the star's energy distributions provided by ESO and by STIS.
The uncertainties in the fluxes of the standard stars and Vega are a few percent. This is combined with the errors (of the same order) in our simulations. Since as we said, the spectral response of the OM U, B and V filters are similar to the standard UBV ones, we have observed the same stars (several hundreds) from the ground and with OM (fields G 153, HD 5980, M67,...) and we have obtained transformations between the two systems (Antokhin, 2002).
In order to be able to switch from the simulated Vega-based values to the values based on observations we needed to apply a correction to the zero points for V, B and U filters. Using the current effective areas (corrected for time sensitivity degradation) these corrections are respectively 0.0131, 0.0232 and 0.0614.
Table 11 gives the final corrected Zero points (ultraviolet and white filters Zero points are based in simulations).

4.2 UBV colour transformation

The transformations from the OM instrumental system to Johnson's system were established based on real observations. As mentioned before, several fields have been observed

from the ground with the standard Johnson UBV filters and with the XMM-Newton OM. (Antokhin et al. 2002 and Antokhin, 2002).
The fitting was limited to stars with less than 20% coincidence loss, and 5% statistical errors leaving a total of 363 cross-identified stars, mostly from the Main Sequence (Antokhin et al. 2002 and Antokhin, 2002).
To calculate the colour-transformations we used the Zero points in Table 11. Within the colour intervals covered by the observational data, the transformations may be described by a second order fit. The transformation equations are given as follows. They have been included in the corresponding SAS CCF file. (The upper case letters denote the Johnson system; the lower case letters the OM system).

$$B - V = -0.0005 + 1.046 \times (b - v) - 0.023 \times (b - v)^2 \quad (6)$$

$$V - v = -0.0008 - 0.006 \times (b - v) - 0.021 \times (b - v)^2 \quad (7)$$

$$B - b = -0.0014 + 0.04 \times (b - v) - 0.044 \times (b - v)^2 \quad (8)$$

$$U - B = -0.002 + 0.901 \times (u - b) + 0.103 \times (u - b)^2 \quad (9)$$

$$B - b = 0.0078 - 0.01 \times (u - b) - 0.019 \times (u - b)^2 \quad (10)$$

$$U - u = 0.046 - 0.109 \times (u - b) + 0.082 \times (u - b)^2 \quad (11)$$

$$U - V = 0.053 + 0.91 \times (u - v) + 0.033 \times (u - v)^2 \quad (12)$$

$$V - v = -0.003 - 0.01 \times (u - v) - 0.004 \times (u - v)^2 \quad (13)$$

$$U - u = 0.048 - 0.097 \times (u - v) + 0.03 \times (u - v)^2 \quad (14)$$

We should point out that not all equations above have been implemented in the SAS. For example, for deriving standard B magnitude, SAS uses (u-b) colour transformation (e.g. 10), or making use of the UV filters (see next section). However, users can also use (b-v) colour transformation (e.g. 8) to get standard B magnitude. In Figure 23, we plot the observed UBV colour-transformation (the red dashed lines), together with the simulated one (crosses and solid lines). By comparing the observed and simulated colour-transformation we can see that the agreements in (B-V, b-v) and (U-V, u-v) are excellent, and the agreements in V-v and B-b are usually better than 2%. The main problem is for the hot stars in the U filter, where the discrepancy can reach 10%. The spectral library (BPGS) used in the simulations is combined from several sources. For the optical data, the spectral atlas is based on Gunn and Stryker (1983) observations, which begins from 313 nm. Colina and Bohlin (1994) have demonstrated that the errors in normalization of the spectra can produce several percent errors in the photometry.

4.3 UV colour transformation

Currently the colour transformations for the UV filters are based on simulations, mainly because of the lack of standard photometry in the UV. However a comparison between the simulated colour-transformations and observational data shows a good agreement.
Some of the simulated UV colour transformation equations are given as follows,

$$B - b = +0.0066 + 1.0085 \times (uvw1 - b) + 0.0031 \times (uvw1 - b)^2 \quad (15)$$

$$V - v = +0.0165 + 1.0059 \times (uvw1 - v) + 0.0009 \times (uvw1 - v)^2 \quad (16)$$

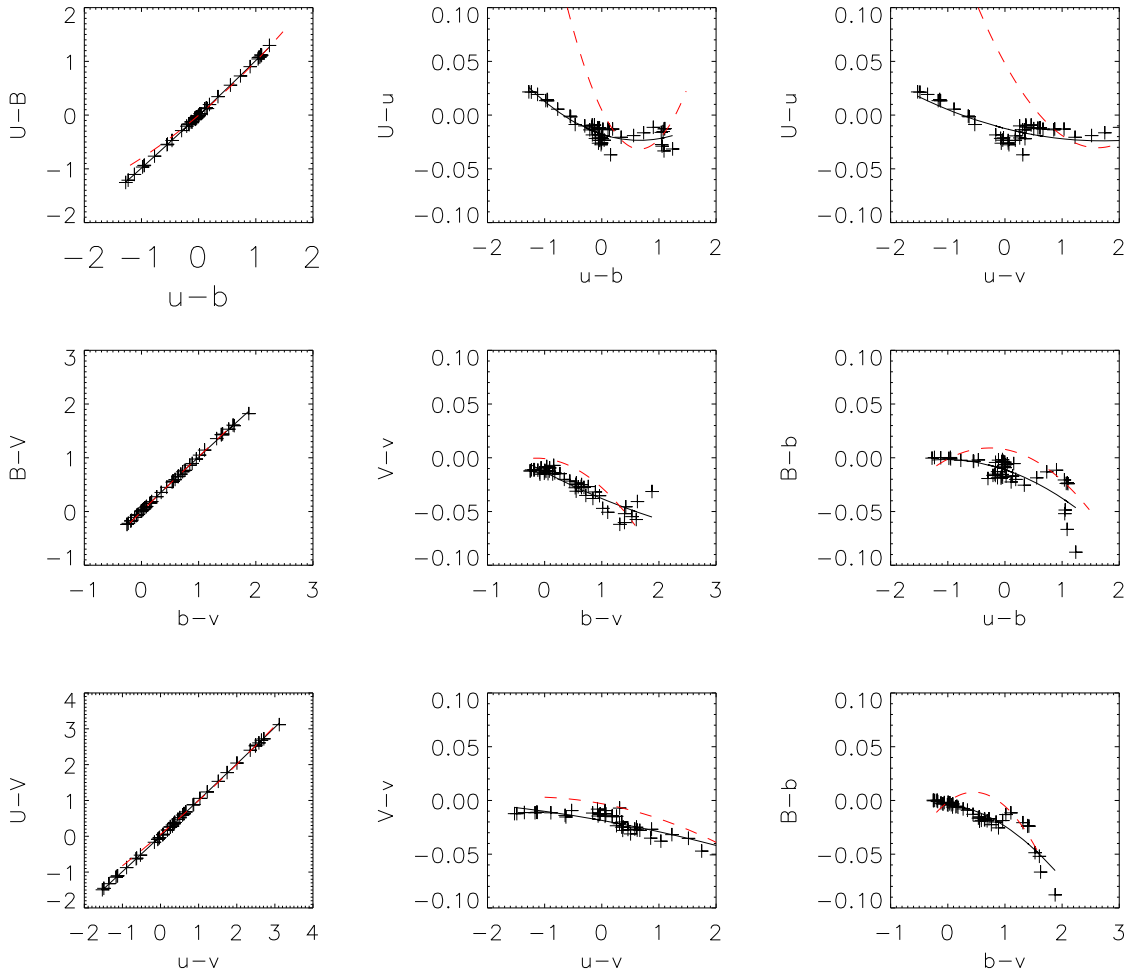


Figure 23: The Observed (the red, dashed lines) and simulated (solid lines and symbols) colour-transformation for U, B and V filters.

Table 12: Zero points in AB system for OM (at zero epoch)

V	B	U	UVW1	UVM2	UVW2
17.9230	19.0809	19.1890	18.5662	17.4120	16.5719

$$U - u = +0.0094 + 1.03325 \times (uvw1 - u) - 0.0233 \times (uvw1 - u)^2 \quad (17)$$

$$U - B = -0.2386 + 0.5383 \times (uvw1 - b) + 0.0157 \times (uvw1 - b)^2 \quad (18)$$

$$B - V = 0.1446 + 0.2761 \times (uvw1 - v) + 0.025 \times (uvw1 - v)^2 \quad (19)$$

Due to observing time constraints or due to bright source restrictions, the optical colours may not be available, in which case these UV colour-transformation can help users to derive the standard UBV magnitudes and colours.

4.4 Testing OM photometry with data in SA95-42 field

A Landolt standard star field (Landolt, 1992), SA95-42, has been observed to test the OM photometric accuracy. Since these standards have very high photometric accuracy ($\sim$ 0.005 mag), the standard deviation on the residuals between the Landolt magnitude and the magnitude derived by OM provides a direct measurement of the OM photometric accuracy. This field is observed with OM fairly regularly.
In Figure 24, we plot the standard V mag differences between Stetson's measurement (Stetson, 2000) and OM measurement in rev. 407 as a function of Stetson standard magnitude. The figure shows that the OM photometric accuracy is 0.023 mag for V filter. Figure 25 shows the standard V mag difference between Stetson's measurement and OM measurement in rev. 759. An offset of 0.04 mag is seen (the dashed line), which does not exist in Figure 24. This can be explained as being due to the time degradation, as shown in Figure 17 - data for this figure do not contain time degradation correction.
We showed in Section 2.8 that the comparison of different observations of this field gave fractional differences between stars of the same order as the measurement errors, thus confirming the stability and consistency of our corrections and calibration.
Figure 26 shows UV colour transformation from two observations, SA95-42 (asterisks) and G153 (diamonds) fields. The dashed line is the colour transformation in the CCF based on the simulations.

4.5 AB photometry system

The AB system (Oke, 1974) can be defined by the response of our instrument to an input spectrum of $1erg/s/cm^2/Hz$. If we obtain in one filter a photon rate n_phot, then the corresponding Zero point is defined as

$$Zero_point = -48.60 - 2.5 \times log10(1/n_phot) \quad (20)$$

Table 12 gives the AB Zero points for OM.

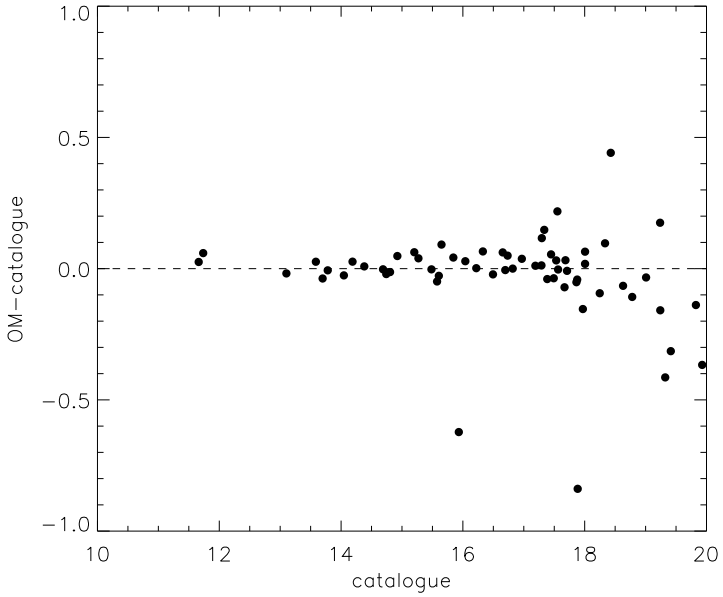


Figure 24: The difference in standard V magnitude between Stetson's measurement and OM measurement for SA95-42 field in rev. 407

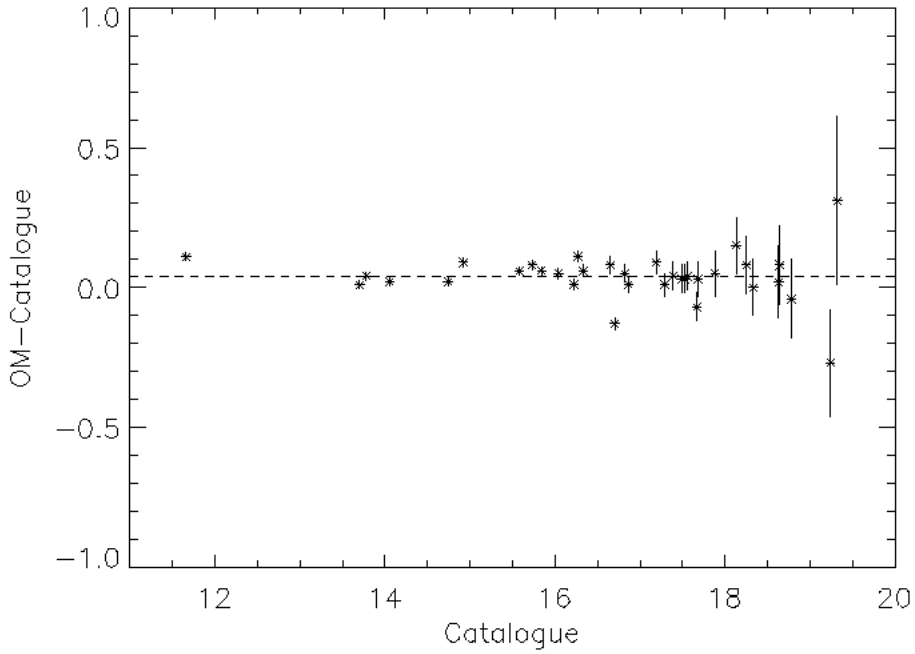


Figure 25: Same as Figure 24 but in rev. 759.

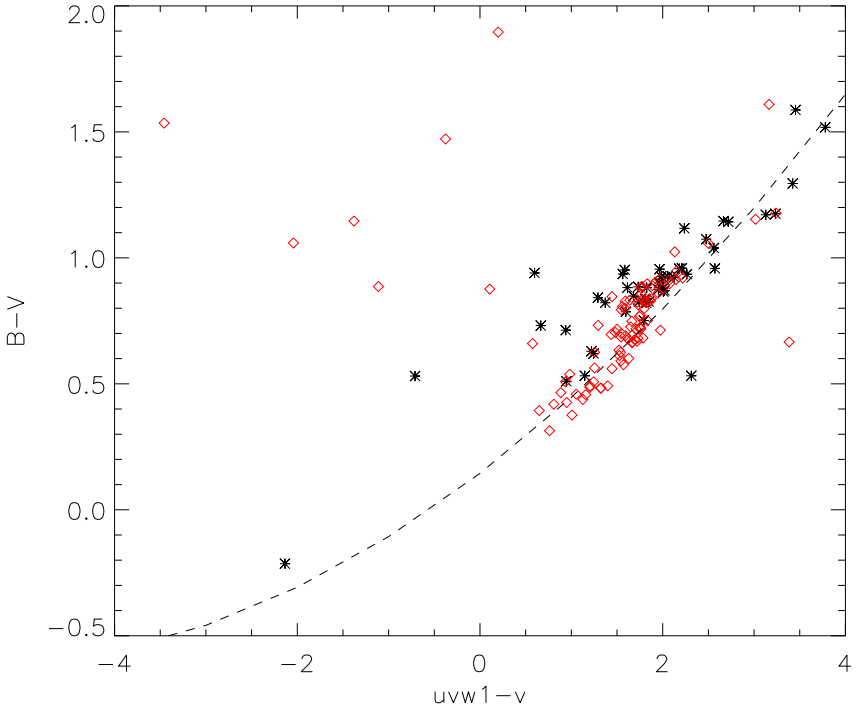


Figure 26: Comparing the observed UV colour-transformation for two fields, SA95-42 (red) and G153 (black), with the simulated one (dashed line).

Table 13: Count rate to flux conversion in AB system (frequency)

uvw2	uvm2	uvw1	u	b	v
8.488e-27	3.911e-27	1.346e-27	7.843e-28	8.396e-28	2.469e-27

(this gives $erg/cm^2/s/Hz$)

If *n_phot* is the number of photons produced by 1 erg input spectrum, then $1/n_phot$ is the count rate to flux conversion factor (in frequency space). Thus the AB system definition provides a simple conversion to flux units in frequency space. It is given in Table 13.

5 Absolute flux calibration of the OM filters (OM count rate to flux conversion)

If we assume that the response curve of the OM filters is flat (almost true for the U, B and V filters) we can derive a count rate to flux conversion that can be applied for all kind of sources, providing that they do not present strong discontinuities it their spectral energy distribution at the band-pass of the OM filters. We can use simulations, including the fudge factor, to compute a mean OM response in each filter, in other words a count to flux conversion factor. We obtain the results given in Table 14. The effective wavelength of the B filter has been arbitrarily set at 4500 Å to avoid the core of the Balmer line Hγ. Alternatively we can observe a series of standard stars with OM (their fluxes can be obtained from the HST CALSPEC database

Table 14: Count rate to flux conversion (from simulations)

filter	UVW2	UVM2	UVW1	U	B	V
lambda (Å)	2120.	2310.	2910.	3440.	4500.	5430.
factor ($erg/cm^2/count/\AA$)	5.66e-15	2.19e-15	4.76e-16	1.97e-16	1.29e-16	2.52e-16

`http://www.stsci.edu/hst/observatory/cdbs/calspec.html`

If we take the standard flux at the effective wavelengths of the OM filters (see Table 15) and their measured count rates, including time sensitivity degradation correction (see Table 16), we can derive a direct count rate to flux conversion factor. After dividing and averaging we obtain the results of Table 17 (quoted relative errors are computed as stdev/mean).

Table 15: Absolute flux of standard stars ($erg/cm^2/s/\AA$)

filter	UVW2	UVM2	UVW1	U	B	V
lambda (Å)	2120.	2310.	2910.	3440.	4500.	5430.
GD153	4.546e-13	3.388e-13	1.517e-13	8.376e-14	3.507e-14	1.733e-14
HZ2	1.350e-13	1.008e-13	5.308e-14	3.215e-14	2.051e-14	1.078e-14
GD50	2.439e-13	1.958e-13	8.094e-14	4.234e-14	1.772e-14	8.879e-15
HZ4	3.781e-14	3.115e-14	1.871e-14	1.221e-14	1.093e-14	6.148e-15
G9348	3.021e-13	2.406e-13	1.153e-13	7.844e-14	5.734e-14	3.048e-14
LTT9491	3.044e-14	3.546e-14	2.462e-14	2.210e-14	1.347e-14	8.751e-15
LBB227	2.566e-14	1.674e-14	1.038e-14	6.489e-15	5.260e-15	2.857e-15

Table 16: Measured count rates of standard stars ($count/s$)

filter	UVW2	UVM2	UVW1	U	B	V
lambda (Å)	2120.	2310.	2910.	3440.	4500.	5430.
GD153	81.45	159.94	325.04	415.68	280.88	70.42
HZ2	22.52	46.09	110.02	162.70	147.80	43.27
GD50	42.63	83.87	178.10	n.a.	n.a.	n.a.
HZ4	6.83	14.23	38.93	n.a.	n.a.	n.a.
G9348	48.17	102.8	257.7	n.a.	n.a.	n.a.
LTT9491	4.82	13.64	56.31	117.8	109.5	34.43
LB227	3.83	7.23	19.61	n.a.	n.a.	11.53

The difference between these factors and the ones obtained from simulations are less than 1 %, an expected result since the simulator is based in the same stars.
We obtained (see Table 13) flux conversion factors in the AB system. Even if we are in frequency space, we can characterize the filter by its effective wavelength. And then we can convert these factors to lambda space by multiplying by (c/λ^2). The results are shown in Table 18.
Not surprisingly, these last factors are very similar to the ones derived directly from WD's fluxes.
These flux conversion factors have been added as keywords FCF* in the COLORMAG extension of the current calibration file (CCF) OM_COLORTRANS. It should be noted

Table 17: Count rate to flux conversion (from standard stars)

filter	UVW2	UVM2	UVW1	U	B	V
lambda (Å)	2120.	2310.	2910.	3440.	4500.	5430.
factor ($erg/cm^2/count/\AA$)	5.71e-15	2.20e-15	4.76e-16	1.94e-16	1.29e-16	2.49e-16
error	0.054	0.0401	0.068	0.042	0.068	0.013

Table 18: Count rate to flux conversion in AB system (wavelength)

filter	UVW2	UVM2	UVW1	U	B	V
lambda (Å)	2120.	2310.	2910.	3440.	4500.	5430.
factor ($erg/cm^2/count/\AA$)	5.67e-15	2.20e-15	4.77e-16	1.99e-16	1.24e-16	2.51e-16

that the flux conversion factors for the AB system currently implemented (calibration file OM_COLORTRANS_0010) are slightly different, because they were based on a former version of the effective area. Since the difference is less than 3% we have not updated the CCF to maintain homogeneity within the XSA and the OM Catalogue. This will be done in a future CCF revision

We should point out that these flux conversion numbers provide an approximate measurement of the flux densities (expressed in $erg/cm^2/s/\AA$) without *a priory* knowledge of the spectral type. Calibration observations have been done to refine the coefficients used in the count rate to flux calculations according to spectral type.

Interested users can visit the SAS watchout page to find flux conversion factors for a given spectral type at:

`https://www.cosmos.esa.int/web/xmm-newton/sas-watchout-uvflux`

6 Fast mode

In fast mode, the OM does not produce accumulated two-dimensional images, but instead produces event lists, like the X-ray instruments. This mode is useful for monitoring rapidly variable sources, for example accreting binaries. One or two windows approximately $11 \times 11 arcsec^2$ can be defined in the detector. Incoming photons in these windows are time tagged. The fastest time sampling is 0.5 s.

As far as instrumental corrections and calibration are concerned, the fast mode data have the same treatment (e.g. aperture photometry) as the image data, except for the difference that, prior to applying the aperture photometry algorithm, the source and background counts extracted from the fast mode window are scaled to the standard photometric aperture (see Section 2.4).

Due to the small size of the fast mode window, the measurement of the source and the background may become very difficult in case of bright targets or when more that one source is present in the window (e.g. crowded fields). In cases of multiple sources found in the fast mode window, the counts belonging to different sources are separated from each other (and, of course, also removed from the background extraction region). As a result, initially, the source and background extraction regions may vary from source to source, so that the counts corresponding to these extraction regions are then scaled to the standard photometric aperture. Of course, the photometric accuracy in the cases of

multiple sources in the fast mode window is lower than in the cases with a single source. It is also unavoidably lower for bright sources because in such cases the whole of the fast mode window is filled in with the source counts and the discrimination between the background and source counts becomes impossible. The most recent version of SAS allows us to measure the background from the image data normally associated with fast mode.
The final product, a light curve, gives the count rate of the source as a function of time in the corresponding filter, with all described corrections applied, except magnitude and flux conversions.
OM fast mode data reduction is fully supported by SAS. For detailed description please refer to the SAS documentation.
An issue that affects fast mode photometry (and also some of the imaging photometry) when using the OM default imaging mode, is a systematic step pattern in the count rates between sub-exposures. This is discussed in appendix C.
Three further issues relating to fast mode are (1) field acquisition (FAQ) failure, which can result in the target being substantially displaced from the window centre at the start of an observation, (2) periodic flux variations arising from spatial oscillations (possibly driven by cyclic heating within the instrument/mounting) when the source is centred very near the edge of the window, and (3) drift between exposures within an observation (especially long observations) where spacecraft or instrument movement can cause a changing fraction of the source PSF to be shifted outside the window. These aspects are described in more detail in a technical note.[2].

7 OM Grisms

For each source the grism gives a dispersed first order image and a zeroth order image, displaced from one another in the dispersion direction. In preparing the observations, default windows are available to select the region of the field of view that will contain the target zero and first order spectra. A full frame low resolution image containing the spectra of all objects in the field of view can also be obtained
Figure 27 shows typical OM Optical grism images obtained in full frame (field spectroscopy) and in a single window around the target spectrum. Zero and first diffraction orders are indicated. The main source is the WD star BPM 16274.
Both UV and optical grisms have been calibrated in wavelength and in flux. Since version 6.0, SAS contains a processing chain and an interactive task that allow the users to extract fully calibrated spectra of the target and all sources in an OM exposure obtained with the grisms. Figure 28 shows the extracted spectrum corresponding to Figure 27
Extracting the spectra from OM grism images with SAS is done as follows:

- The raw image is corrected from modulo_8 fixed pattern noise. Then, the geometrical distortion introduced by the OM detector is corrected by using the distortion map, available through OM_ASTROMET CCF. The undistorted image is rotated so as to align the dispersion direction with the image columns.
- A detection algorithm is used to search for all spectra, zero and first orders, in the image. Then these detections are correlated to assign to each zero order its

[2]https://xmmweb.esac.esa.int/docs/documents/CAL-TN-0224.pdf

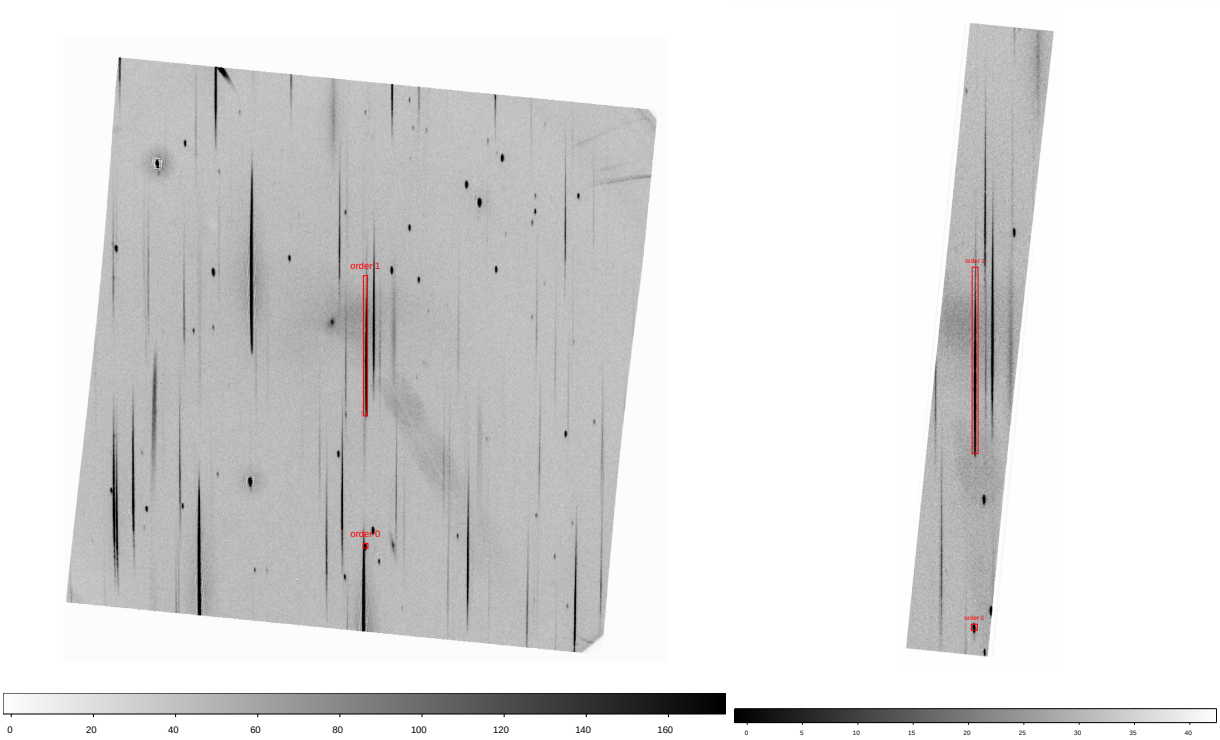


Figure 27: The BPM16274 field taken with the optical grism. Left: the full field of view. Right: a window around the target.(Original images have been rotated to align the image columns with the dispersion direction.)

corresponding first order. Spectral extraction is performed on the successful cases.

- The positions of the zero orders of the extracted spectra are used to derive the astronomical coordinates of the corresponding sources. This is particularly useful in case of field spectroscopy when OM is used in full frame mode with the grisms. Matching the positions of the zero orders with their corresponding positions in a direct image requires an additional distortion map for each grism. (See Section 2.7.)

- The extracted spectra are calibrated in wavelength and in absolute flux.

As we have said before, the reader is referred to the SAS documentation for details on the complete grism data reduction.

7.1 Wavelength calibration

The dispersion relations have been obtained by observing several F type stars for the UV grism, and a DA2 white dwarf (BPM 16274) for the Visible grism. The wavelength scales are provided as a function of the distance (X) in pixels (at full resolution) from the centroid of the zeroth order in the extracted spectrum
For the Visible grism, we have

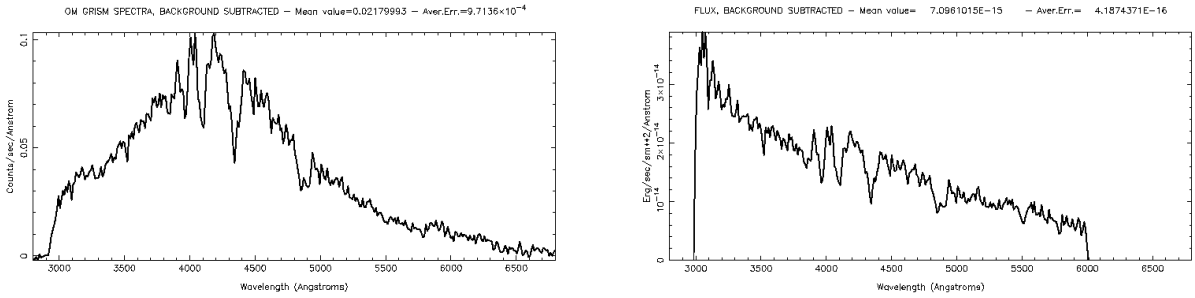


Figure 28: The BPM16274 spectrum taken with the optical grism. Left: raw spectrum. Right: flux calibrated spectrum. Hydrogen Balmer lines are clear.

$$\lambda(\mathring{A}) = 5.626 \times X + 200.898 \pm 7.5 \tag{21}$$

and for the UV grism,

$$\lambda(\mathring{A}) = 0.000771 \times X^2 + 1.866 \times X + 991.778 \pm 2.0 \tag{22}$$

Uncertainties in measuring the position of the zeroth order may produce a shift in the scale of ± 10 Å for the UV grism and ± 20 Å for the visible grism.
The applied fixed pattern modulo 8 noise correction is not perfect, particularly for the visible grism. This effect limits the spectral resolution of the OM grisms, which is better than 15 Å at 2600 Å for the UV grism (and worse than that for the visible one).

7.2 Flux calibration

The observation with OM of GD 153 and Hz 2, both spectroscopic standard stars (white dwarfs) allowed us to measure the throughput of the grisms and to derive an inverse sensitivity function (ISF) which can be used to convert the count rate in the extracted spectrum into absolute flux units

$$Flux(\lambda) = S_OM(\lambda) \times ISF(\lambda) \tag{23}$$

where S_OM is the OM extracted spectrum (count rate units)
The ISF for both grisms is presented in Figure 29.
To obtain the ISF, several observations of GD 153 and Hz 2 performed with both OM grisms have been used. All data have been processed with SAS. The extracted spectra in count rate versus wavelength have been compared with the spectral energy distribution of the stars obtained from the HST Calspec database.
In Figure 30 we present the ISF under the form of effective area for both OM grisms.
Wavelength calibration and ISFs are included in the calibration file OM_GRISMCAL for their use within SAS.
It should be noted that the UV grism is not blazed. This produces an overlapping of the first and second orders, which can be very important for hot objects. The contamination free spectral range extends from 1800 Å to 3600Å.
This is the range for which its flux calibration has been derived.

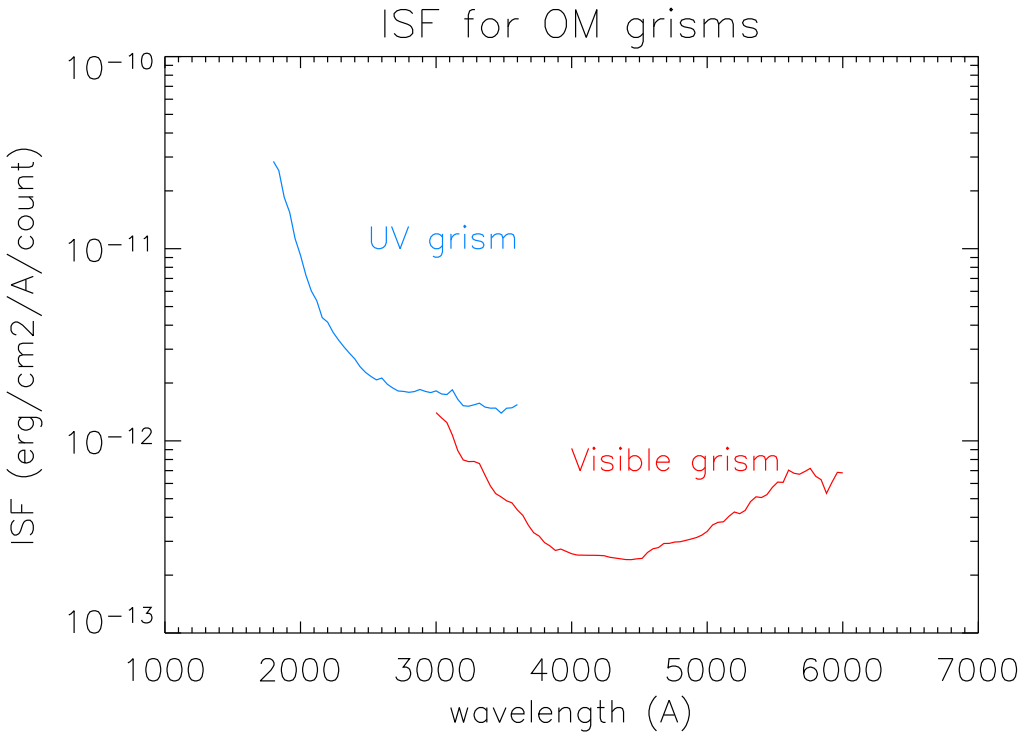


Figure 29: The OM grisms Inverse Sensitivity Function (ISF)

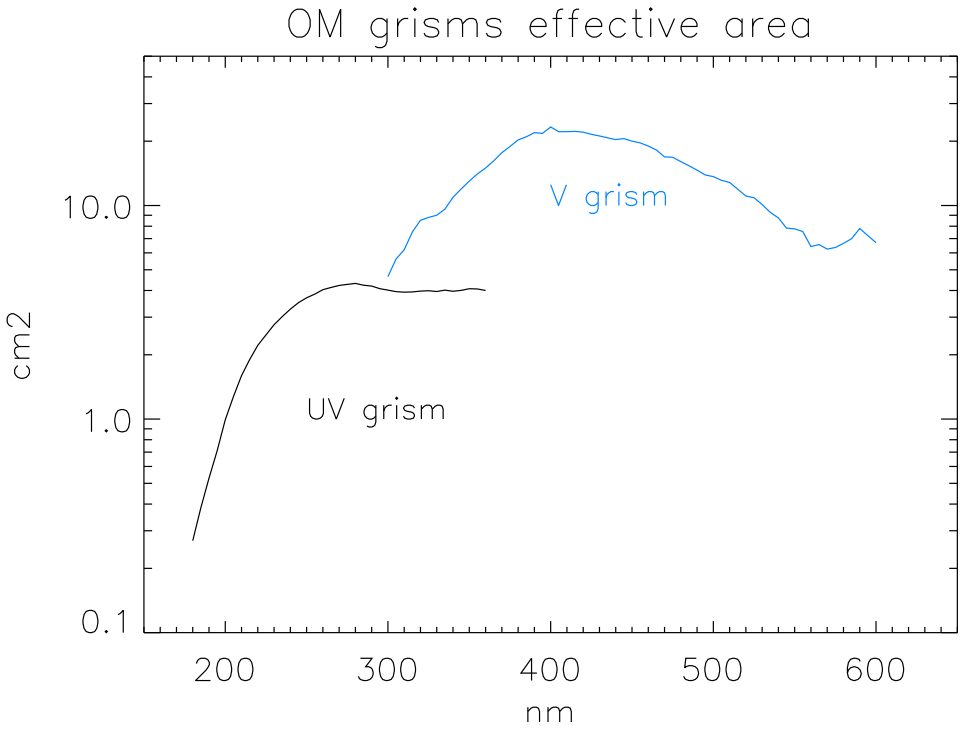


Figure 30: The effective area of the OM grisms

Figure 31 shows the spectra of the three white dwarf standard stars BPM 16274, Hz 2 and GD 153 obtained with OM, compared with its corresponding standard flux. The flux observed in each OM filter, after converting count rates to flux, is shown also in this figure.
The excellent agreement between both grisms in their common wavelength range (3000 - 3600 Å)should be noted, and also the agreement with the optical and UV filters.
The flux calibration stars observations are not affected (or very slightly) by coincidence losses. This effect is not corrected yet in the processing of grisms data with SAS, thus very bright sources will have large errors.

7.3 Time-dependent degradation

Grism data suffer from the effects of time-dependent sensitivity degradation (TDS), in a similar way to the photometric data (section 3.1). The degradation in the grism data was first characterised in 2018.
With much more limited OM grism data, the analysis is based on a set of 3 standard stars. Separately, for each of the UV and visible grisms, spectra of the 3 standard stars, BPM16274, GD153 and Hz2 are extracted from all available observations over the mission baseline. Count rates are extracted from 6 wavelength bands in each grism, discarding any affected by quality issues, such as contamination by other spectra or zeroth order features. Although there is undoubtedly a wavelength dependence to the degradation, as there is for the photometry, due to the noise and scatter present in the grism data, at the current time the analyses effectively combine the band data to determine a band-averaged decline. For each grism, the measurements from each star and each band are then fitted simultaneously, with linear functions (adequate for the current data) that have a common slope but whose normalisations are band and star dependent, i.e. $R_{s,b}(t) = A_{s,b}(1 + B.t)$ where $R_{s,b}(t)$ is the measured rate in band, b, for star, s, at time t (measured relative to epoch 2000.0 (MJD 51544.0), 3 weeks after the launch of XMM), $A_{s,b}$ is the normalisation at t=2000.0 for the star and band, and B is the common slope. The fits obtained to the data are shown in figure 32, after normalisation of each star/band count rate measurement by the relevant $A_{s,b}$ value. Note that for the UV grism, the data from BPM16274 were excluded because, being significantly fainter than Hz2 and GD153, its spectrum is noisier and does improve the accuracy of the fit.
Thus a single decline slope is determined for each grism. The values determined in 2025 are shown in table 19. The functions are evaluated at a set of uniformly spaced time grid points and inverted to obtain the correction values, which are stored in the OM_GRISMCAL CCF. Correction values derived in 2025, for the 2000-2028 epoch range, are shown in table 20[3]. Since SAS 18, the OM grism SAS software applies the TDS correction to a grism spectrum, by interpolation of the CCF data. Note that only the final fluxed spectrum is corrected in the grism spectrum products - the rates are *not* corrected.
Since the fits yield quite small (significantly < 1) reduced χ^2 values, the uncertainties on the corrections at 2025 were estimated from simulations, and are 1.8% and 1.7% for the UV and visible grisms respectively.

[3]see also https://xmmweb.esac.esa.int/docs/documents/CAL-SRN-0413-1-0.pdf

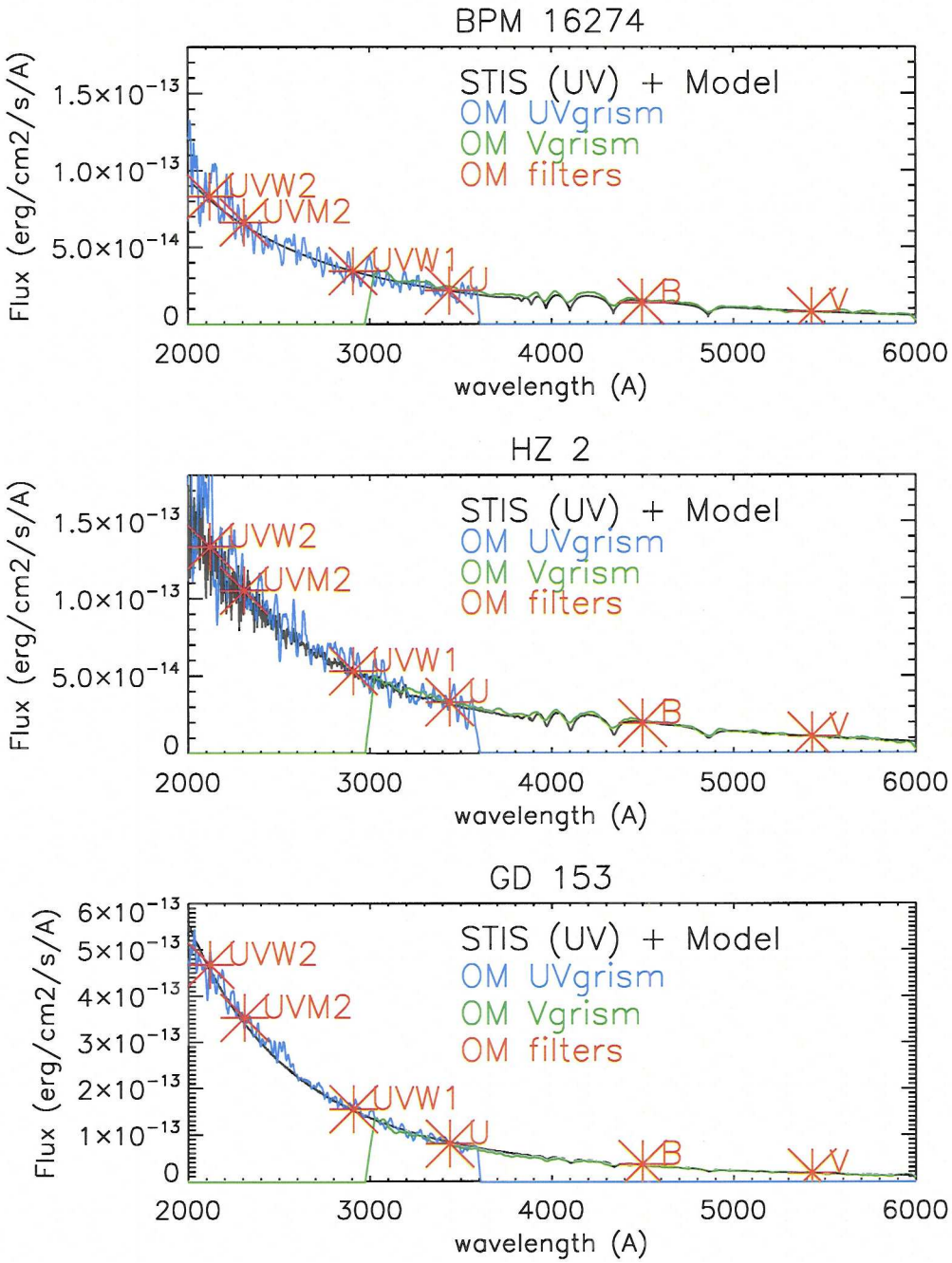


Figure 31: Flux calibrated spectra of the standard stars BPM 16274, Hz 2 and GD 153 obtained with the OM grisms and lenticular filters

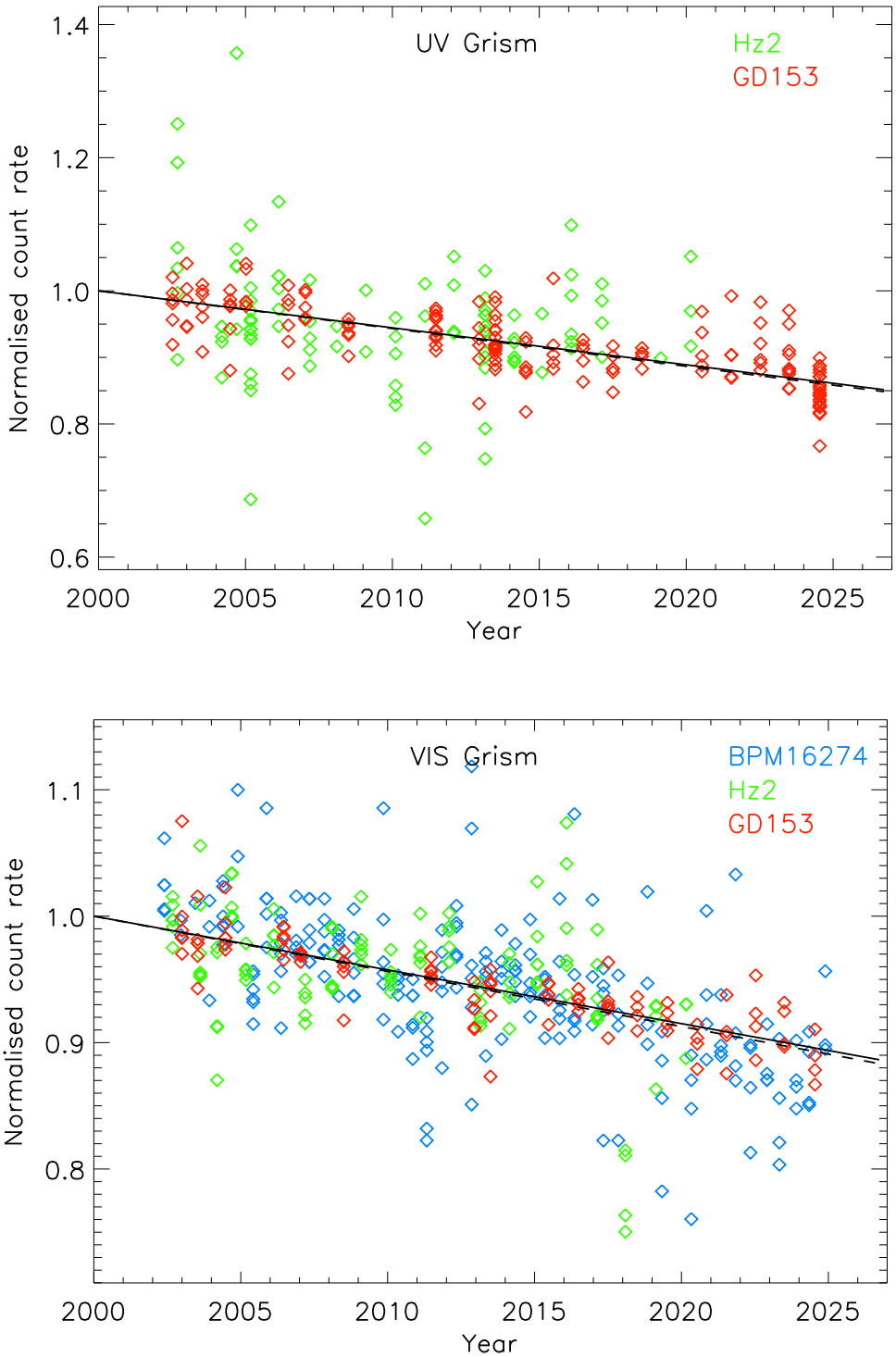


Figure 32: Upper panel: Measurements of the 6 band count rates from the UV grism observations of Hz2 and GD153 (band values are not distinguished in the plot) - data from BPM16274 were excluded from the analysis as it is notably fainter, and thus noisier than the other two sources and adds little to the accuracy of the fit). Each point (for a given band and star) is normalised by the relevant rate of that band and star at mission start, derived from simultaneous fitting of all the data. Lower panel: As for the upper panel, but for the visible grism (and including data from BPM16274). In each panel, the solid black line is the fit obtained from all data up to

Table 19: Slopes for the linear sensitivity degradation trends of the OM grisms

Grism	Slope
UV	-0.005557
Visible	-0.004249

Table 20: Corrections factors for the average time-dependent sensitivity degradation in the OM grisms

Year	UV Grism	Visible Grism
2000	1.000	1.000
2002	1.011	1.009
2004	1.023	1.017
2006	1.034	1.026
2008	1.047	1.035
2010	1.059	1.044
2012	1.071	1.054
2014	1.084	1.063
2016	1.098	1.073
2018	1.111	1.083
2020	1.125	1.093
2022	1.139	1.103
2024	1.154	1.114
2026	1.169	1.124
2028	1.184	1.135

7.3.1 Impact of the Jupiter patch

Many OM grism observations or target objects are made using a pre-defined default window configuration, as mentioned in section 7. Spectra of such targets taken since the Jupiter observation (see section 2.2.1), generally cross the localised elliptical patch of diminished sensitivity caused by the event.
For such cases observed at epochs after revolution 3224, users should thus be aware that a portion of the spectrum of a target source will be affected by this patch. In the UV grism, data in the 2120Å - 2600Å range are affected, with a maximum degradation of ≈25% at 2350Å, while for the Visible grism, the 3440Å - 4180Å range is affected, with a maximum impact also of about 25%, at 3860Å. Figure 33 shows part of a UV grism image of GD153, where the Jupiter patch can clearly be seen as a darker elliptical region, while figure 34 shows the extracted flux spectrum of the source, displaying a clear depression around 2400Å, due to the patch.
The impact of the JDP is not currently corrected in SAS or pipeline processing. It should also be noted that the amount of degradation can depend sensitively on the exact location of the spectrum (in particular, where it crosses the major axis of the patch) since the degradation in the patch has a strong spatial dependence.

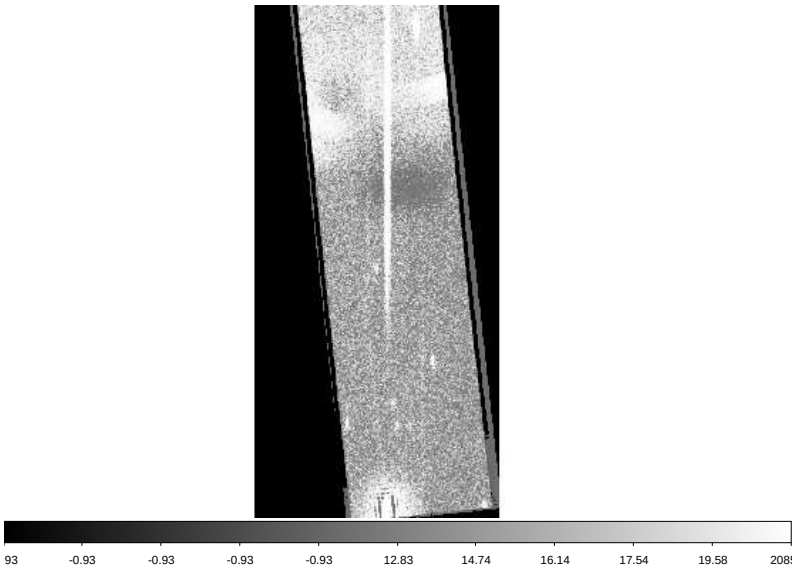


Figure 33: OM UV grism image of GD153, observed after the Jupiter observation - the spectrum lies across the dark region of degraded sensitivity caused by the Jupiter observation

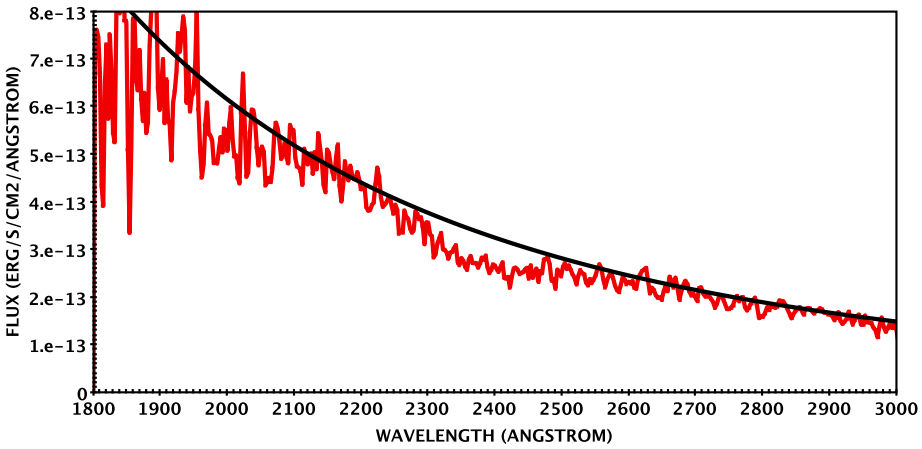


Figure 34: Fluxed OM UV grism spectrum of GD153 from the image in 33. The impact of the Jupiter patch is visible as the depression centred near 2400Å. The black line is an estimated power-law fit to the data either side of the dip.

8 Current Calibration Files (CCFs) for SAS

Table 21 provides a list of the OM calibration files. The SAS tasks using a given CCF are indicated as well. For a detailed description of these files and of their usage, the user is referred to the CCF interface document and to the Calibration Access and Data Handbook

`https://xmm-tools.cosmos.esa.int/external/xmm_calibration/calib/documentation/CALHB/index.html`

Table 21: Calibration files of the Optical Monitor.

File name	File Content	SAS task
ASTROMET	coefficients for geometric distortion correction	omatt omdetect omdrifthist omgprep
BADPIX	bad pixels position, type of defect and the severity level	omcosflag omfastflat
BORESIGHT	alignment of the instruments and star tracker	omatt omgprep
COLORTRANS	zero points, coefficients for color transformation into a standard system count rate to flux conversion	ommag omdetect omlcbuild
GRISMCAL	wavelength & flux calibrations for the grisms, and TDS degradation correction table	omgrism
HKPARMINT	house keeping parameter ranges	ommag
LARGESCALESENS	flat field map (set to unity)	omflatgen
PHOTTONAT	correction coefficients of count rates for detector non-linearity and aging, and TDS correction coefficients	ommag omprep omdetect omlcbuild
PIXTOPIXSENS	flat field map (set to unity)	omflatgen
PSF1DRB	point spread function for each filter	ommag omdetect omlcbuild

9 Future calibration plans

Most of the calibration items have been covered in this description. All of them have been incorporated into the standard data reduction done with SAS, other than corrections for the Jupiter patch.
A few refinements and some new developments are under investigation or consideration. Among them:

- Understanding and rectifying the cause of differences seen in count rates observed from objects repeatedly observed in the image and fast mode data taken in default mode. This issue, which is probably associated with the coincidence-loss correction, is discussed further in appendix C.
- Resolving the cause of a difference seen in the time-dependent sensitivity decline of the OM catalogue sources and of the standard stars. The decline is shallower for the standards by around 2-5% in the V and UVW2 filters. This topic is described further in appendix D
- Ultimately, obtaining a full, filter-dependent and spatially-dependent characterisation of the sensitivity degradation in the Jupiter patch is desired, to allow both image correction and correction for photometry obtained from sources within the patch.
- Extending the time dependent sensitivity analysis in the grisms to include wavelength dependence
- Calibrating wavelength variation in the UV grism, across the detector
- Refining the characterisation of large scale sensitivity variations

10 Acknowledgments

We thank all the people who have contributed to the operation and calibration of XMM-OM. This includes many people at MSSL (Alice Breeveld, Cynthia James, Tracey Poole, Elizabeth Auden, Keith Mason, Chris Brindle, Vladimir Yershov, Mat Page, Martin Still), Liege University (Igor Antokhin), UCSB (Tim Sasseen, Bob Shirey, Jamie Kennea), ESTEC (Rudi Much) and ESAC (Nora Loiseau, Eva Verdugo, María Diaz, Bing Chen, Jan Uwe Ness, Antonio Talavera). We thank also the Mission Planning and Mission Operations Teams at ESAC and ESOC, without whose support the mission (and calibration) would not be possible.

11 References

Antokhin I., Breeveld A., Chen B., et al. 2002, ESA SP-488, Proc. Symposium *'New Visions of the X-ray Universe in the X MM-Newton and Chandra Era'*
Antokhin I., 2002, Internal Report to the OM Calibration Team.
Breeveld A.A., Curran P.A., Hoversten E.A. et al, 2010, MNRAS, 406, 1687
Colina L., Bohlin R.C., 1994, AJ, 108, 1931
Gunn J.E., Stryker L.L., 1983, ApJ Supplement, 51, 121
Kirsch M.G. et al, 2005, Proc. SPIE, Vol 5898, 212
Landolt A. U., 1992, AJ, 104, 340
Mason K.O., Breeveld A.A., Much R.M. et al. 2001, A&A 365, L36
Mason K.O., 2002, ESA SP-488, ESTEC, The Netherlands
Oke J.B., ApJS, 27, 21
Page, M., 2012, MNRAS, 426, 903P

Poole T.S., 2006, MSSL Internal Report
Stetson P. B., 2000, PASP, 112, 925

12 Appendix A: Calibration stars

Table 22 lists the sources used in the calibration of OM

Table 22: Stars used in the Calibration of the Optical Monitor.

Star name	**Type**	**Purpose**
BPM 16274	DA..	time sensitivity variations, wavelength of Visible grism
HZ 2	DA3 D	time sensitivity variations, grisms flux, effective area, zero points, count rate to flux conversion
GD 153	DAw...	time sensitivity variations, grisms flux, effective area,zero points, count rate to flux conversion
GD 50	DA D	effective area, zero points, count rate to flux conversion
HZ 4	DA: D	effective area, zero points, count rate to flux conversion
G93-48	DA3 D	effective area, zero points, count rate to flux conversion
LTT 9491	DC D	effective area, zero points, count rate to flux conversion
LB 227	DA: D	effective area, zero points, count rate to flux conversion
SA 95-42	Landolt standard field	photometry, large scale sensitivity
EXO 0748-67	star field	large scale sensitivity
G 153	star field	colour transformations, geometric distortion
HD 5980	star field	colour transformations
M 67	cluster	colour transformations
HD 13499	F5V	UV grism wavelength
HD 221996	F5V	UV grism wavelength
HD 224317	F5V	UV grism wavelength
Sco X1	star field	geometric distortion of grisms

13 Appendix B: Summary of errors and repeatability

Table 23 gives the errors of the different calibration items of OM.

Table 23: Errors in the Calibration of the Optical Monitor.

Astrometry

	mean offset (arcsec)	standard deviation (arcsec)
Right Ascension	-0.36	1.5
Declination	0.54	1.6

Photometry

Magnitudes	V, B : 2%	U: 10%
Flux conversion	2% to 7% depending on filter	

Grisms Spectroscopy

Wavelength	Visible grism (Å)	UV grism (Å)
	7.5	2.0
	Possible offset up to 20 Å	
Flux	Less than 10 % - Worst at the long wavelength end	

As part of the routine calibration observations we use three standard stars, GD 153, Hz 2 and BPM 16274. Table 24 shows a summary of 16, 18 and 36 observations of these stars respectively. All data have been processed with SAS 18.0 applying all corrections described in this document.
It can be seen that measurements of the standards, performed along the life of the instrument, show scatter (standard deviations) in each filter of less than 3.5%, most being less than 2%. We note that the data of the standards are corrected for time-dependent sensitivity loss based on analysis of the 'constant' bulk sources in the OM catalogue (see section 3.1) but we draw attention to the fact that in the V and UVW2 filters, the uncorrected count rates of the standards decline more slowly than the bulk sources after 2010, by as much as ∼5%. One anticipates that the corrected timeseries of the standards should be statistically flat as they are constant sources but as their count rates in table 24 are corrected using the steeper declines measured in the bulk source, this yields rising corrected count rates for the standards after 2010 in the V and UVW2 filters, and this is the cause of the enhanced scatter (standard deviation or percentage error in the table) seen in these two filters. This is further discussed in appendix D.

14 Appendix C: Flux steps in Fast mode and imaging photometry taken in default mode

Exposures taken in default imaging mode comprise 5 temporally sequential sub-exposures, each sub-exposure consisting of 2 windows: one is a large, low resolution (LR) (1" x 1" pixels) window that covers a different part of the field of view in each sub-exposure while the other is a high resolution (HR) (0.5" x 0.5" pixel) one, 1.9' x 1.9' on a side, that covers the same region at the centre of the field of view each time. In addition, up to 2 fast mode windows may be used in each sub-exposure.

Table 24: OM measured count rate (cts/s) repeatability

	GD 153			Hz 2			BPM 16274		
filter	mean	stdev	error(%)	mean	stdev	error(%)	mean	stdev	error(%)
UVW2	83.47	1.44	1.7	23.87	0.53	2.2	14.75	0.25	1.7
UVM2	162.1	2.4	1.5	48.31	0.60	1.2	30.31	0.31	1.0
UVW1	330.8	4.5	1.3	111.9	1.4	1.3	72.90	0.70	1.0
U	421.6	6.2	1.5	168.8	1.5	0.9	112.6	0.8	0.7
B	283.9	2.7	0.9	148.7	1.3	0.9	107.7	1.0	0.9
V	71.60	1.63	2.3	44.07	1.52	3.4	33.18	0.82	2.5

It has been found that the count rate measurements of brighter sources measured in the 5 repeated central HR windows, and from the fast mode windows (if used), show a systematic up-down-up-down step pattern of several percent (notably more prominent in the fast mode data), that is independent of any intrinsic source variability. An example is shown in figure 35. While there is some intrinsic source variability present, the step pattern is clear and amounts to a $(max - min)/mean$ ∼4% in the imaging data and ∼10% in the fast mode data. Similar effects are seen in the data of standard stars where intrinsic variability is absent.

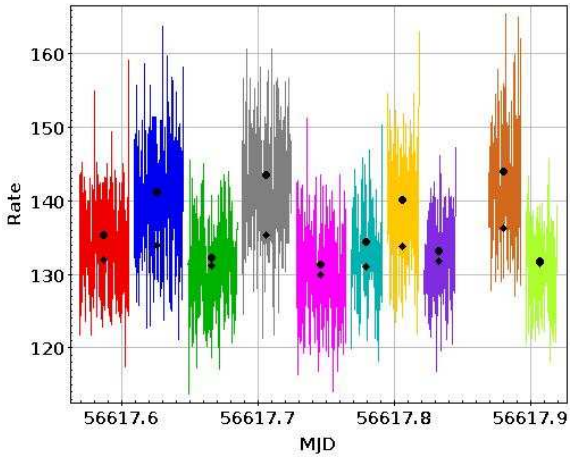


Figure 35: UVW2 fast-mode timeseries from 2 default mode exposures (10 sub-exposures) from a source in observation 0728200201. Overlayed on these are the similarly corrected mean count rates measured from the corresponding fast mode images (filled black circles), and from the larger HR central imaging mode images (filled black diamonds) from the same sub-exposure. The data have been corrected for coincidence loss and any PSF corrections, in the standard manner. The amplitude of the residual variation in the fast mode data is substantially higher than in the HR imaging data.

The key differences between each sub-exposure in a default mode set are the frame-time and dead-fraction. This is because the frame-time and dead fraction of a sub-exposure depend on the largest Y-axis boundary of any of the windows in it and, as the larger LR

window of each pair in a sub-exposure has a different location, the frame-time changes with sub-exposure. In principle, the coincidence-loss correction takes account of this (see section 2.5) but there appears to be a residual, unresolved issue that affects the correction. A further effect, possibly related to the PSF corrections, appears to amplify the effect in fast mode data. Analysis is ongoing to isolate the underlying causes of the step effects and will be reported, via a technical note, once identified and addressed.
It should be noted that, due to this step pattern issue, use of the default mode for fast mode timing studies is now deprecated: users are steered to use the user-defined mode where frame times and dead fractions are the same between exposures. Nevertheless, a solution to the above-mentioned issue is still sought, to correct archival data taken in the default mode.

15 Appendix D: Differences between the time-dependent degradation seen in standards and OM catalogue sources

In section 3.1 it was mentioned that the analysis of the TDS degradation correction is now performed using data from serendipitous stars that are deemed constant in the OM catalogue, supplanting the original approach of using standard stars. It is, however, also evident from figure 21, where the time series measurements of BPM16274 are corrected for the degradation derived from the 'constant' catalogue sources, that in the V and UVW2 bands, the standard star count rates rise from about 2010 (rev 1800), whereas, being a standard star, we would expect them to be constant. This rise, which is as much as 6%, is seen in each of the 3 main standard stars, and, to a lesser extent, in some Landolt standards in the SA95 field.
The cause of this rising trend is not yet resolved. While it is natural to assume that standard stars, being constant sources, should provide the most reliable measure of the degradation, other potential factors, such as spatially localised sensitivity effects (especially perhaps, at the boresight where the standards, and target sources, have generally been observed), mean the standards can not necessarily be taken as definitive. As noted in section 2.8, no clear evidence was found for large-scale variations in sensitivity and so none are incorporated into the flat-field map, but the spatial scales sampled could well miss small localised effects. The statistical constraints on the flat-field measurements and the pixel-to-pixel variations (section 2.2) also mean an unrecognized variation of up to about 5% could be present. Indeed if a localised sensitivity effect were a factor, use of sources that sample the whole detector would, in principle, be more appropriate for determining the general degradation. Nevertheless, there are arguments against localised sensitivity degradation being the cause.
At the present time, this issue remains under investigation and when the cause is understood and/or conclusions are reached, they will be reported through a technical note.

16 Appendix E: Corrections for the additional degradation at the pn boresight

As discussed in section 3.4, the extra degradation at the pn boresight, due to the Jupiter patch, can be corrected, approximately, using measurements of the standard stars. Be-

low we present a tabulated form of the correction values, for each filter, for a grid of revolutions.

Table 25: Correction factors, for each filter, for correcting count rates of sources at the pn boresight for the extra degradation. Values are given for a fixed grid of modified Julian dates. These values can be linearly interpolated for other epochs. Points beyond revolution 4284 (MJD 60065) represent an extrapolation of the correction function but as this is nearly linear since rev 3224, the implied correction for epochs > rev 4284 should be accurate to better than 1%. However, note also that the numerator (LTT) used in computing the correction curve involves offset data taken after the Jupiter observation. There is an uncertainty associated with this of up to ∼2% in the V filter, due to the uncertainty in the constant residual level of the exponential (in the absence of a full characterisation of any time and filter dependent spatial sensitivity variations, we can not rule out some differences in the rates measured at offset locations relative to the pn boresight). Nevertheless, extrapolating the fits obtained from the pre-JO boresight data alone, shows consistency with the offset data, in all filters, within about 2%

MJD	V	B	U	UVW1	UVM2	UVW2
57951.0	1.0766	1.0643	1.0544	1.0541	1.0168	1.0442
58001.0	1.0783	1.0656	1.0553	1.0546	1.0172	1.0450
58051.0	1.0800	1.0670	1.0562	1.0551	1.0175	1.0458
58101.0	1.0817	1.0684	1.0571	1.0556	1.0179	1.0466
58151.0	1.0835	1.0698	1.0580	1.0562	1.0182	1.0474
58201.0	1.0852	1.0712	1.0589	1.0567	1.0186	1.0482
58251.0	1.0870	1.0727	1.0599	1.0572	1.0190	1.0491
58301.0	1.0887	1.0741	1.0608	1.0577	1.0194	1.0499
58351.0	1.0905	1.0755	1.0617	1.0583	1.0198	1.0507
58401.0	1.0923	1.0770	1.0627	1.0588	1.0202	1.0516
58451.0	1.0941	1.0784	1.0636	1.0593	1.0206	1.0525
58501.0	1.0959	1.0799	1.0646	1.0599	1.0210	1.0533
58551.0	1.0977	1.0814	1.0656	1.0604	1.0214	1.0542
58601.0	1.0995	1.0828	1.0665	1.0610	1.0219	1.0551
58651.0	1.1013	1.0843	1.0675	1.0615	1.0223	1.0560
58701.0	1.1031	1.0858	1.0685	1.0621	1.0228	1.0569
58751.0	1.1050	1.0873	1.0695	1.0627	1.0232	1.0578
58801.0	1.1068	1.0888	1.0705	1.0632	1.0237	1.0587
58851.0	1.1087	1.0904	1.0714	1.0638	1.0241	1.0597
58901.0	1.1106	1.0919	1.0724	1.0644	1.0246	1.0606
58951.0	1.1124	1.0934	1.0735	1.0650	1.0251	1.0615
59001.0	1.1143	1.0950	1.0745	1.0656	1.0255	1.0625
59051.0	1.1162	1.0965	1.0755	1.0662	1.0260	1.0634
59101.0	1.1181	1.0981	1.0765	1.0668	1.0265	1.0644
59151.0	1.1200	1.0997	1.0775	1.0674	1.0270	1.0654
59201.0	1.1219	1.1013	1.0786	1.0680	1.0275	1.0663
59251.0	1.1238	1.1028	1.0796	1.0686	1.0281	1.0673
59301.0	1.1258	1.1044	1.0807	1.0692	1.0286	1.0683
59351.0	1.1277	1.1060	1.0817	1.0699	1.0291	1.0693
59401.0	1.1297	1.1077	1.0828	1.0705	1.0296	1.0703
59451.0	1.1316	1.1093	1.0838	1.0711	1.0302	1.0713

MJD	V	B	U	UVW1	UVM2	UVW2
59501.0	1.1336	1.1109	1.0849	1.0718	1.0307	1.0723
59551.0	1.1356	1.1126	1.0860	1.0724	1.0313	1.0734
59601.0	1.1376	1.1142	1.0870	1.0731	1.0319	1.0744
59651.0	1.1396	1.1159	1.0881	1.0737	1.0324	1.0754
59701.0	1.1416	1.1175	1.0892	1.0744	1.0330	1.0765
59751.0	1.1436	1.1192	1.0903	1.0750	1.0336	1.0775
59801.0	1.1456	1.1209	1.0914	1.0757	1.0342	1.0786
59851.0	1.1476	1.1226	1.0925	1.0764	1.0348	1.0797
59901.0	1.1496	1.1243	1.0936	1.0770	1.0354	1.0808
59951.0	1.1517	1.1260	1.0947	1.0777	1.0360	1.0818
60001.0	1.1537	1.1277	1.0959	1.0784	1.0366	1.0829
60051.0	1.1558	1.1294	1.0970	1.0791	1.0372	1.0840
60101.0	1.1579	1.1311	1.0981	1.0798	1.0378	1.0852
60151.0	1.1599	1.1329	1.0993	1.0805	1.0385	1.0863
60201.0	1.1620	1.1346	1.1004	1.0812	1.0391	1.0874
60251.0	1.1641	1.1364	1.1015	1.0819	1.0398	1.0885
60301.0	1.1662	1.1381	1.1027	1.0826	1.0404	1.0897
60351.0	1.1683	1.1399	1.1039	1.0833	1.0411	1.0908
60401.0	1.1705	1.1417	1.1050	1.0840	1.0417	1.0920
60451.0	1.1726	1.1435	1.1062	1.0848	1.0424	1.0931
60501.0	1.1747	1.1453	1.1074	1.0855	1.0431	1.0943
60551.0	1.1769	1.1471	1.1086	1.0862	1.0438	1.0955
60601.0	1.1790	1.1489	1.1097	1.0870	1.0445	1.0966
60651.0	1.1812	1.1507	1.1109	1.0877	1.0452	1.0978
60701.0	1.1833	1.1526	1.1121	1.0885	1.0459	1.0990
60751.0	1.1855	1.1544	1.1133	1.0892	1.0466	1.1002
60801.0	1.1877	1.1563	1.1146	1.0900	1.0473	1.1014
60851.0	1.1899	1.1581	1.1158	1.0907	1.0480	1.1027
60901.0	1.1921	1.1600	1.1170	1.0915	1.0488	1.1039
60951.0	1.1943	1.1619	1.1182	1.0923	1.0495	1.1051
61001.0	1.1965	1.1637	1.1194	1.0931	1.0503	1.1064
61051.0	1.1988	1.1656	1.1207	1.0938	1.0510	1.1076
61101.0	1.2010	1.1675	1.1219	1.0946	1.0518	1.1089
61151.0	1.2033	1.1694	1.1232	1.0954	1.0525	1.1101